Sterol scarcity primes p38 immune defenses through a TIR-1/SARM1 phase transition

Nicholas D. Peterson[1,#], Janneke D. Icso [2,#], J. Elizabeth Salisbury[1], Tomás Rodríguez[3], Paul R. Thompson[2,*] Read Pukkila-Worley[1,*]

[1]Program in Innate Immunity, Division of Infectious Diseases and Immunology, University of Massachusetts Medical School, Worcester, MA, 01655, United States of America

[2]Department of Biochemistry and Molecular Pharmacology, University of Massachusetts Medical School, Worcester, MA, 01655, United States of America

[3]RNA Therapeutics Institute, University of Massachusetts Medical School, Worcester, MA, 01655, United States of America

#These authors contributed equally to this work

*Correspondence may be addressed to Read Pukkila-Worley (Read.Pukkila-Worley@umassmed.edu, @RPWlab) or Paul Thompson (Paul.Thompson@umassmed.edu, @pthompsn1018)

Classification: Major: Biological Sciences; Minor: Immunology and Inflammation

Keywords: p38 pathway; cholesterol; TIR-1/SARM1; phase transition

ABSTRACT

Intracellular signaling regulators can be concentrated into membrane-free, higher-ordered protein assemblies to initiate protective responses during stress — a process known as phase transition. Here, we show that a phase transition of the *C. elegans* Toll/interleukin-1 receptor domain protein (TIR-1), a homolog of the mammalian sterile alpha and TIR motif-containing 1 (SARM1), primes host immune defenses when dietary sterols are limited to handle subsequent bacterial infection. TIR-1/SARM1 is an upstream component of the p38 PMK-1 pathway in intestinal cells, an innate immune defense and stress response pathway in metazoans. Under conditions of low cholesterol availability, multimerization and precipitation of TIR-1/SARM1 potentiates the intrinsic NAD^+ glycohydrolase activity of this protein complex, increases p38 PMK-1 phosphorylation, and promotes pathogen clearance from the intestine. Dietary cholesterol is required for *C. elegans* to survive infection with pathogenic bacteria and to support development, fecundity, and lifespan. Thus, activation of the p38 PMK-1 pathway in sterol-deficient animals is an adaptive response that allows a metazoan host to anticipate environmental threats under conditions of essential metabolite scarcity.

41 **SIGNIFICANCE STATEMENT**

42 The nematode *C. elegans* must consume dietary sterols to support growth and reproduction.
43 However, access to dietary sterols in its natural habitat is not guaranteed and thus, nematodes
44 have evolved mechanisms to promote survival in sterol-poor environments. Here, we demonstrate
45 that activation of the p38 PMK-1 innate immune pathway in response to low sterol availability
46 promotes clearance of a bacterial pathogen from the intestine. Pre-emptive activation of innate
47 immune defenses occurs through a phase transition of TIR-1/SARM1, an upstream component
48 of the p38 PMK-1 pathway, which activates its intrinsic NAD^+ glycohydrolase activity. Thus,
49 nematodes anticipate threats from infectious pathogens during a time when the animal is relatively
50 susceptible to infection.

51 **INTRODUCTION**

52 Access to essential dietary metabolites alters the life history traits of metazoans. For
53 example, *Caenorhabditis elegans* lack the ability to synthesize cholesterol *de novo* and must
54 acquire dietary sterols from its environment to support development, fecundity, lifespan, and
55 resistance against pathogen infection (1-7). *C. elegans* larvae that encounter sterol-scarce
56 environments are primed to enter an alternative developmental program, called dauer diapause,
57 which promotes animal survival, in part, by altering their metabolism and growth to conserve
58 energy (8-12). Interestingly, only a fraction of sterol-starved *C. elegans* larvae enter dauer
59 diapause and the remaining animals develop to adulthood (10, 13). Thus, *C. elegans* that do not
60 enter dauer diapause must adapt during sterol scarcity to develop and reproduce.

61 The p38 mitogen-activated protein kinase (MAPK) pathway is a key regulator of stress
62 responses and innate immune defenses in metazoans. The *C. elegans* p38 homolog PMK-1 is
63 part of a classic MAPK signaling cascade that is activated by the MAPKKK NSY-1 and MAPKK
64 SEK-1, which are the nematode homologs of mammalian ASK and MKK3/6, respectively (14). *C.*
65 *elegans* Toll/interleukin-1 receptor domain protein (TIR-1), which is homologous to mammalian
66 sterile alpha and TIR motif-containing 1 (SARM1), acts upstream of NSY-1 to control p38 PMK-1
67 activation (15, 16). As in mammals, the *C. elegans* p38 PMK-1 pathway regulates the expression
68 of secreted innate immune effectors and is required for survival during pathogen infection (14, 17-
69 19). However, the mechanisms that activate the NSY-1/SEK-1/p38 PMK-1 signaling cassette in
70 *C. elegans* intestinal epithelial cells are poorly defined.

71 Intracellular signaling regulators can be compartmentalized in membrane-less, higher-
72 ordered protein assemblies with liquid droplet-like properties (20-26). Cytoplasmic de-mixing or
73 phase transition of proteins in this manner concentrates signaling regulators to facilitate rapid and
74 specific activation of protective defenses during stress (20, 21, 27). Here, we show that TIR-
75 1/SARM1 undergoes a phase transition to potentiate its intrinsic NAD^+ glycohydrolase activity and
76 activate innate immune defenses in intestinal epithelial cells via the p38 PMK-1 pathway. By

77 promoting aggregation of TIR-1/SARM1 with macromolecular crowding agents *in vitro*, we
78 demonstrate that a phase transition of TIR-1/SARM1 is required for its catalytic activity.
79 Accordingly, TIR-1/SARM1 containing mutations that specifically either prevent the phase
80 transition or impair NAD^+ hydrolysis have decreased enzymatic activity *in vitro* and are unable to
81 activate the p38 PMK-1 pathway *in vivo*. Importantly, we show that limiting dietary sterols primes
82 p38 PMK-1 immune defenses, in a manner dependent on a phase transition of TIR-1/SARM1, to
83 promote clearance of a bacterial pathogen from the intestine. Availability of dietary cholesterol is
84 required for *C. elegans* to survive infection with pathogenic bacteria (6). Thus, activation of the
85 p38 PMK-1 pathway through a TIR-1/SARM1 phase transition during conditions of sterol scarcity
86 is an adaptive response in animals that fail to enter dauer diapause. Immune activation, in this
87 manner, primes host immune defenses to promote clearance of a bacterial pathogen from the
88 intestine during a period of relative vulnerability to infection.

RESULTS

Cholesterol scarcity activates intestinal innate immune defenses.

C. elegans are sterol auxotrophs and require dietary cholesterol for development, lifespan, fecundity, and resistance to pathogen infection (1-7). As such, 5 µg/mL of cholesterol is a standard additive in *C. elegans* laboratory growth medium (28). We found that *C. elegans* grown in the absence of cholesterol supplementation activated GFP-based transcriptional reporters for two putative immune effector genes, T24B8.5p::*gfp* and *irg-5*p::*gfp* (Fig. 1*A* and *B*). T24B8.5 and *irg-5* are expressed in the intestine, induced during infection with multiple pathogens—including *Pseudomonas aeruginosa,* and controlled by the p38 PMK-1 innate immune pathway (17, 29, 30). qRT-PCR studies confirmed that *C. elegans* in a low cholesterol environment upregulate T24B8.5 and *irg-5,* as well as other innate immune effector genes (*irg-4* and K08D8.4) (Fig. 1*C*). These data suggest that host defense pathways are activated in the absence of pathogen infection when environmental sterols are scarce.

The nuclear hormone receptor, NHR-8, a homolog of mammalian liver X receptor (LXR) and pregnane X receptor (PXR), is required for the transport, distribution, and metabolism of cholesterol in *C. elegans* (13, 31). We used two previously characterized *nhr-8* loss-of-function mutant strains as genetic tools to study conditions of low sterol content: *hd117*, which contains a 570 base pair deletion that removes the entire first exon (13), including the start codon, and *ok186*, a strain that contains a 1366 base pair deletion that removes most of the ligand-binding domain (31). The *nhr-8(hd117)* loss-of-function mutant has lower total cholesterol levels and is unable to develop under conditions of cholesterol deprivation (13). Interestingly, both *nhr-8(hd117)* and *nhr-8(ok186)* animals grown under standard conditions (*i.e.*, in the presence of 5 µg/mL cholesterol) induce a transcriptional response, which mimics wild-type *C. elegans* infected with the bacterial pathogen *P. aeruginosa* (Fig. 1*D* and S1*A*). RNA-sequencing (RNA-seq) revealed that the differentially expressed genes in uninfected *nhr-8(hd117)* (Fig. 1*D* and Table S1) and *nhr-8(ok186)* (Fig. S1*A* and Table S1) mutants (each versus wild-type animals) significantly correlated

115 with genes that are differentially expressed in wild-type animals during infection with *P.*
116 *aeruginosa* (r = 0.311 and r = 0.370, respectively). These correlations increase when comparing
117 only the genes whose transcription are significantly differentially regulated (r = 0.763 and r =
118 0.849, respectively) and those genes that are also involved in innate immunity (r = 0.677 and r =
119 0.703, respectively) (Fig. 1*D* and S1*A*). Among the immune effectors that are upregulated in *nhr-*
120 *8(hd117)* and *nhr-8(ok186)* mutants are T24B8.5, *irg-4*, *irg-5*, and K08D8.4, the same genes
121 whose transcription are also induced during cholesterol deprivation (Fig. 1*C*, 1*D* and S1*A*).

122 Two different supplementation experiments using the T24B8.5p::*gfp* immune reporter
123 demonstrated that immune effector activation in *nhr-8(hd117)* mutants is due to sterol deficiency
124 in these animals. First, supplementation of exogenous cholesterol at an increased concentration
125 (80 µg/mL) fully suppressed T24B8.5p::*gfp* activation in the *nhr-8(hd117)* mutant (Fig 1*E*).
126 Second, supplementation with the non-ionic detergents Tergitol or Triton X-100, which solubilize
127 hydrophobic, amphipathic compounds, including sterols, suppressed T24B8.5p::*gfp* activation in
128 *nhr-8(hd117)* animals, in a manner that was dependent on the presence of added cholesterol in
129 the growth media (Fig. 1*F-G* and S1*B*). Nematode growth media without supplemented
130 cholesterol is not entirely devoid of sterols, owing to sterol contamination from agar. However,
131 growth media solidified with agarose, rather than agar, contains markedly fewer contaminating
132 sterols (2, 10, 13). Interestingly, on agarose, the addition of Tergitol to the growth media
133 suppressed T24B8.5p::*gfp* activation in the *nhr-8(hd117)* mutant, but only in the presence of 5
134 µg/mL of cholesterol (Fig. 1*G*). These data establish that solubilization of cholesterol by Tergitol
135 in standard nematode growth media suppresses immune activation in the *nhr-8(hd117)* mutant
136 background. Suppression of T24B8.5p::*gfp* activation in the *nhr-8(hd117)* background by Tergitol
137 and Triton X-100 was dose-dependent (Fig. S1*B*). Supporting these findings, Tergitol suppressed
138 activation of the immune effector genes T24B8.5, *irg-4*, *irg-5* and K08D8.4 in the *nhr-8(hd117)*
139 animals as measured by qRT-PCR (Fig. 1*H-K*). Of note, activation of immune defenses in *nhr-*
140 *8(hd117)* animals is specific to cholesterol deprivation in this genetic background, as

141 supplementation with individual unsaturated, mono- and polyunsaturated fatty acids, which are
142 also mis-regulated in the *nhr-8(hd117)* mutant background (13), failed to suppress activation of
143 T24B8.5p::*gfp* (Fig. S1*C*). Together, these data demonstrate that cholesterol deprivation in the
144 *nhr-8(hd117)* mutant activates immune effector transcription independent of bacterial infection.

145 *C. elegans* raised on media without supplemented cholesterol are hypersusceptible to
146 killing by *P. aeruginosa*, as are *nhr-8(hd117)* mutants on media with standard cholesterol
147 supplementation (5 µg/mL) (6). We found that 80 µg/mL of cholesterol fully complemented the
148 enhanced susceptibility of *nhr-8(hd117)* mutants to *P. aeruginosa* infection (Fig. 1*L*). In addition,
149 solubilizing cholesterol in nematode growth media containing 5 µg/mL of added cholesterol with
150 two different detergents restored pathogen resistance to the *nhr-8(hd117)* mutant (Fig. 1*M*).
151 Consistent with a prior report, we found that *nhr-8* is required in the intestine for resistance to
152 pathogen infection (6). Knockdown of *nhr-8* only in intestinal epithelial cells enhanced the
153 susceptibility of *C. elegans* to pathogen infection (Fig. S1*D*). In addition, expression of *nhr-8* either
154 under the control of its own promoter (Fig. S1*E*) or under the control of a promoter (*ges-1*) that
155 drives expression specifically in intestinal epithelial cells complemented the pathogen
156 susceptibility of *nhr-8(hd117)* animals (Fig. S1*F*). We showed that expression of *nhr-8* only in
157 neurons, under the control of the *sng-1* promoter, failed to rescue the susceptibility of *nhr-*
158 *8(hd117)* animals to *P. aeruginosa* infection (Fig. S1*G*). Taken together, these data demonstrate
159 that defects in cholesterol metabolism in intestinal epithelial cells specifically causes *C. elegans*
160 to be more susceptible to killing by a bacterial pathogen.

161 Importantly, the robust transcriptional induction of immune effectors observed in the *nhr-*
162 *8(hd117)* mutant (Fig. 1*A*-*B* and 1*D*) promotes clearance of *P. aeruginosa* from the intestine even
163 though these mutant animals are more susceptible to pathogen killing (Fig. 1*N*). These data
164 suggest that *C. elegans* activates host immune defenses when environmental sterols are limited
165 to anticipate subsequent lethal challenges from bacterial pathogens.

166

167 **Cholesterol scarcity activates the p38 PMK-1 innate immune pathway.**

168 *C. elegans* propagated in the absence of cholesterol engage the transcription of genes
169 that are targets of the p38 PMK-1 innate immune pathway (Fig. 1*C*). Consistent with this
170 observation, the levels of active, phosphorylated PMK-1 were higher in wild-type animals grown
171 on media without supplemented cholesterol than in animals grown under standard culture
172 conditions (*i.e.*, with 5 µg/mL cholesterol), as assessed by immunoblotting with antibodies that
173 detect the doubly phosphorylated TGY motif of PMK-1 (active PMK-1) and the total PMK-1 protein
174 (32) (Fig. 2*A* and *B*). These data demonstrate that cholesterol deprivation activates p38 PMK-1.

175 The p38 PMK-1 pathway is also activated in *nhr-8* loss-of-function mutants. A gene set
176 enrichment analysis of the *nhr-8(hd117)* and *nhr-8(ok186)* transcriptome profiling experiments
177 revealed that the transcriptional targets of the p38 PMK-1 innate immune pathway were strongly
178 enriched among the genes upregulated in each *nhr-8* mutant (Fig. 2*C* and S2*A*), including the
179 immune effectors T24B8.5, *irg-4*, *irg-5*, and K08D8.4. Consistent with these data, the *nhr-*
180 *8(hd117)* and *nhr-8(ok186)* mutants had an increased ratio of phosphorylated PMK-1 relative to
181 total PMK-1 compared to wild-type controls (Fig. 2*D* and 2*E*). In addition, RNAi-mediated
182 knockdown of *tir-1*, the most upstream component of the p38 signaling cassette (15, 16), fully
183 suppressed hyperactivation of T24B8.5p::*gfp* in *nhr-8(hd117)* animals (Fig. 2*F*). Consistent with
184 these data, the *tir-1(qd4)* loss-of-function mutation completely suppressed the induction of
185 T24B8.5, *irg-4*, *irg-5*, and K08D8.4 in the *nhr-8(hd117)* background (Fig. 2*G*-*J*). The transcription
186 factors ATF-7 and SKN-1 link PMK-1 activity to its transcriptional outputs (33, 34). In *nhr-8(hd117)*
187 animals, knockdown of *atf-7*, but not *skn-1,* abrogated T24B8.5p::*gfp* activation (Fig. 2*F* and S2*B*).
188 Finally, to further support our observation that cholesterol scarcity induces immune defenses
189 upstream of p38 PMK-1, we used the MAPK phosphatase *vhp-1*, a negative regulator of PMK-1
190 (35). Solubilization of cholesterol with Tergitol was unable to suppress activation of T24B8.5p::*gfp*
191 induced by knockdown of *vhp-1* (Fig. 2*K*). Thus, the TIR-1-p38 PMK-1-ATF-7 signaling axis is
192 activated in the *nhr-8* mutant background.

193 The c-JUN N-terminal kinase MAPK homolog *kgb-1*, the insulin signaling pathway
194 forkhead box O family (FOXO) transcription factor, *daf-16*, and the G protein-coupled receptor
195 (GPCR), *fshr-1*, each function in parallel to the p38 PMK-1 pathway to regulate immune and stress
196 responses in *C. elegans* (17, 35-37). However, knockdown of each of these genes in *nhr-8(hd117)*
197 animals failed to suppress T24B8.5p::*gfp* activation (Fig. S2*B*) and RNAi-mediated knockdown of
198 *nhr-8* did not induce nuclear localization of DAF-16::GFP (Fig. S2*C*). Thus, cholesterol scarcity
199 induces *C. elegans* innate immune responses through specific activation of p38 PMK-1 immune
200 pathway signaling.
201
202 **Activation of the p38 PMK-1 pathway by cholesterol deprivation requires TIR-1**
203 **oligomerization and NAD^+ glycohydrolase activity.**
204 *C. elegans* TIR-1, which is homologous to mammalian SARM1, functions upstream of the
205 MAPKKK NSY-1; MAPKK SEK-1; MAPK p38 PMK-1 signaling cassette in the intestine to control
206 innate immune defenses (15, 38). Accordingly, *tir-1* loss-of-function mutants are more susceptible
207 to killing by *P. aeruginosa* than wild-type animals (15). The TIR-1 protein has three characterized
208 domains: a Heat/Armadillo repeat domain, a sterile alpha motif (SAM) domain, and a Toll-
209 interleukin receptor (TIR) domain (38) (Fig. 3*A*). *C. elegans* TIR-1 oligomerizes *in vitro* through
210 interactions of its SAM domains (39). In addition, oligomerization of SARM1 is essential for its
211 function in plants and mice (39, 40). As such, we examined if oligomerization of *C. elegans* TIR-
212 1 is required to activate the p38 PMK-1 immune pathway in the intestine. We used CRISPR-Cas9
213 to delete both SAM domains in *tir-1* (*tir-1*$^{\Delta SAM}$) (Fig. 3*A*). We also generated point mutants in two
214 residues within the *C. elegans* TIR domain that are important for the self-association and activity
215 of mammalian SARM1 (*C. elegans tir-1*^{G747P} and *tir-1*^{H833A}) (39) (Fig. 3*A*). Interestingly, the *C.*
216 *elegans tir-1*$^{\Delta SAM}$*, tir-1*^{G747P} and *tir-1*^{H833A} mutants prevented activation of the p38 PMK-1-
217 dependent immune reporter T24B8.5p::*gfp* in *nhr-8(RNAi)* animals (Fig. 3*B*). Importantly,
218 induction of T24B8.5p::*gfp* during cholesterol scarcity was also absent in these mutants (Fig. 3*C*).

219 Consistent with these data, the *tir-1*$^{\Delta SAM}$*, tir-1*^{G747P} and *tir-1*^{H833A} mutants have reduced levels of
220 active, phosphorylated p38 PMK-1, equivalent to the *tir-1(qd4)* null allele (29) (Fig. 3*D* and *E*).
221 Additionally, they abrogate the induction of the T24B8.5 (Fig. 3*F*) and *irg-4* (Fig. S3*A*) immune
222 effectors in *nhr-8(RNAi)* animals and are each markedly hypersusceptible to *P. aeruginosa*
223 infection (Fig. 3*G*).

224 The TIR domain of *C. elegans* TIR-1 and its mammalian homolog SARM1 possess
225 intrinsic NADase activity (39, 41, 42). Importantly, oligomerization of mammalian SARM1 and *C.*
226 *elegans* TIR-1 is required for maximal NADase activity *in vitro* (39). The NADase activity in the
227 TIR domain of mammalian SARM1 requires a putative catalytic glutamate residue (42). We used
228 CRISPR-Cas9 to mutate the homologous catalytic glutamate residue in *C. elegans tir-1* (*tir-1*^{E788A})
229 and found that it was required for the immunostimulatory activity of *tir-1. tir-1*^{E788A} mutants were
230 unable to induce T24B8.5p::*gfp* both following knockdown of *nhr-8* (Fig. 3*B*) and also during
231 cholesterol scarcity (Fig. 3*C*). Likewise, the *tir-1*^{E788A} mutant animals had less active,
232 phosphorylated p38 PMK-1 (Fig. 3*D* and *E*), completely suppressed the induction of T24B8.5
233 (Fig. 3*F*) and *irg-4* (Fig. S3*A*), and were more susceptible to *P. aeruginosa* infection (Fig. 3*G*). We
234 confirmed that the *tir-1*^{E788A}, *tir-1*$^{\Delta SAM}$*, tir-1*^{G747P} and *tir-1*^{H833A} mutants are translated and not
235 degraded by introducing a 3X FLAG tag at the C-terminus of each of these mutants using
236 CRISPR-Cas9 (Fig. S3*B* and *C*). A western blot with an anti-FLAG antibody yielded a band of the
237 expected size for each of the *tir-1* mutants (Fig. S3*B*). Collectively, these data provide genetic
238 evidence that oligomerization of TIR-1 and its intrinsic NADase activity are required to activate
239 the p38 PMK-1 innate immune pathway.

240

241 **The NAD$^+$ glycohydrolase activity of TIR-1/SARM1 is activated by a phase transition**

242 To characterize further the mechanism of TIR-1/SARM1 activation, we recombinantly
243 expressed and purified from *E. coli* the TIR domain of the TIR-1 protein (called TIR) and evaluated

244 its NADase activity *in vitro* using an etheno-NAD^+ (ε-NAD) activity assay, in which hydrolysis of
245 the nicotinamide ring of ε-NAD leads to an increase in fluorescence. Interestingly, purified TIR
246 only shows very modest NADase activity even at high protein concentrations (>15 μM) (Fig. 4*A*).
247 Notably, the NADase activity of TIR increased parabolically with increasing TIR concentrations
248 rather than linearly, suggesting that multimerization of TIR-1 potentiates its NADase activity (Fig.
249 4*A*).

250 Given that high concentrations of TIR are required to observe NADase activity, we
251 hypothesized that molecular crowding might activate the enzyme and therefore assessed the
252 effect of several macro- and microviscogens on TIR activity. Macroviscogens reduce the free
253 volume available for protein movement and thus promote aggregation of protein complexes that
254 are capable of self-association (43, 44). Importantly, macroviscogens have minimal impact on the
255 rate of diffusion of small molecules. By contrast, microviscogens, which are much smaller than
256 most enzymes, affect the diffusion of substrates in solution and thus, the frequency at which
257 enzymes encounter their substrate (44). Interestingly, macroviscogens (polyethylene glycol [PEG]
258 3350 and PEG 8000), but not microviscogens (sucrose or glycerol), dramatically increased the
259 NADase activity of TIR (Fig. 4*B*). PEGs 3350 and 8000 increase TIR activity in a concentration-
260 dependent manner (Fig. 4*C*). These effects were most pronounced with higher molecular weight
261 PEGs as treatment with smaller molecular weight PEGs (e.g., PEG 1500 and PEG 400) or dextran
262 did not increase the enzymatic activity of TIR (Fig. 4*C*). Crowding agents also increase the activity
263 of the TIR domain of human SARM1, as well as plant TIR domains (39, 45), suggesting that the
264 mechanism of TIR regulation is strongly conserved.

265 Treatment with macroviscogens enabled the characterization of the enzyme kinetics of
266 TIR. Incubation with 25% PEG 3350 markedly enhances TIR activity at each enzyme
267 concentration (Fig. S4*A*). Consequently, lower amounts of enzyme (2.5 μM TIR) can be used to
268 obtain robust kinetic data. Using these conditions, we determined the steady-state kinetic

269 parameters (k_{cat}, K_M, and k_{cat}/K_M) with 2.5 μM TIR in the presence of increasing concentrations of
270 PEG 3350 (Fig. 4*D*). The K_m of TIR increases and then decreases to level off at ~500 μM of ε-
271 NAD with increasing concentration of PEG 3350 (Fig. 4*E*). On the other hand, k_{cat} increases near
272 linearly with increasing concentrations of PEG 3350 (Fig. 4*F*). In addition, the catalytic efficiency
273 (k_{cat}/K_m) followed the same trend as k_{cat}, indicating that increased TIR activity is due to increased
274 substrate turnover by the enzyme and not tighter substrate binding (Fig. 4*G*).

275 We found that the NAD hydrolase activity of TIR is also activated by the precipitant sodium
276 citrate, providing an orthologous method to characterize the enzymatic activity of the TIR domain
277 (Fig. S4*A* and *B*). Notably, the response to increasing citrate concentration was switch-like, where
278 a concentration of at least 250 mM sodium citrate was needed to observe enzyme activity (Fig.
279 S4*B* and S4*C*). By contrast, activation with PEG 3350 was more dose-dependent (Fig. 4*C* and
280 *D*). Nevertheless, the kinetic parameters obtained in the presence of citrate displayed similar
281 trends to those found with PEG 3350: K_m decreased to level off at ~400 μM of ε-NAD (Fig. S4*D*),
282 k_{cat} increases with increasing sodium citrate concentration (Fig. S4*E*), and k_{cat}/K_m follows the k_{cat}
283 trends (Fig. S4*F*).

284 In the cytoplasm, high concentrations of macromolecules (proteins, nucleic acids, lipids,
285 carbohydrates) cause molecular crowding and induce phase transitions of signaling proteins (46).
286 To determine if TIR undergoes a phase transition and whether NADase activity correlates with
287 the transition, we incubated purified TIR with different concentrations of PEG3350 or citrate,
288 centrifuged the sample, and evaluated TIR NADase activity in the soluble and insoluble fractions
289 (Fig. 4*H* and S4*G*). At low concentrations of both PEG and citrate, TIR protein was present in the
290 supernatant. However, at high concentrations of both PEG and citrate, TIR was principally located
291 in the pelleted (insoluble) fraction, as visualized by Coomassie staining on an SDS-PAGE gel
292 (Fig. 4*H* and S4*G*). Importantly, NADase activity was not detected in the supernatant of samples
293 treated with high concentrations of PEG or citrate, whereas robust NADase activity was observed

294 in the pelleted fraction (Fig. 4*H* and S4*G*). Taken together, these data demonstrate that
295 precipitation of TIR is required to activate the intrinsic NADase activity of TIR-1/SARM1.

296

297 **TIR phase transition and NAD^+ glycohydrolase activity requires TIR oligomerization.**

298 To determine whether TIR-1 oligomerization is also required for a phase transition and the
299 NADase activity of TIR, we recombinantly expressed and purified from *E. coli* the TIR domain of
300 TIR-1 containing mutations in residues required for oligomerization (TIR^{G747P}) and NAD^+ catalysis
301 (TIR^{E788A} and TIR^{E788Q}). Notably, the catalytic efficiency (k_{cat}/K_m) of TIR^{G747P}, TIR^{E788A} and TIR^{E788Q}
302 mutants was decreased 10-fold compared to TIR^{WT} (Fig. 4*I*). Kinetic analysis of the recombinant
303 TIR mutants in 25% PEG 3350 revealed that the K_m of ε-NAD increases 2-fold and the k_{cat}
304 decreases 4-fold compared to TIR^{WT} (Fig. 4*I*). These data demonstrate that the decreased activity
305 of the TIR mutants is due to a combination of both decreased substrate binding and decreased
306 substrate turnover. Similarly, kinetic analysis of TIR oligomerization and catalytic mutants in 500
307 mM citrate revealed that the catalytic efficiency (k_{cat}/K_m) decreases by 4-12-fold, similar to trends
308 we observed in experiments conducted with PEG 3350 (Fig. S4*H*).

309 To further characterize the TIR phase transition, we evaluated the precipitation capacity
310 of TIR oligomerization and catalytic mutants in the presence of PEG 3350 and citrate. Consistent
311 with our genetic data, TIR^{G747P}, which contains a mutation that prevents oligomerization of TIR,
312 was unable to precipitate as readily as TIR^{WT} (Fig. 4*J*). Compared to TIR^{WT}, the TIR^{G747P} mutant
313 in the presence of PEG 3550 demonstrated a 25% decrease in the amount of precipitated protein
314 (Fig. 4*J*). We observed similar results in the presence of citrate, in which compared to TIR^{WT}, the
315 TIR^{G747P} mutant demonstrated a 22% decrease in precipitated protein compared to TIR^{WT} (Fig.
316 S4*I*). Importantly, TIR proteins with two different mutants in the catalytic glutamate required for
317 NAD^+ catalysis, TIR^{E788A} and TIR^{E788Q}, precipitated to a similar extent as TIR^{WT} (Fig. 4*J*-*K* and S4*I*-

318 *J*), but had minimal NADase activity (Fig. 4*I* and S4*H*). Collectively, these data demonstrate that
319 a phase transition of TIR-1 is required for its NADase activity.

320

321 **A phase transition superactivates the intrinsic NAD^+ glycohydrolase activity of TIR.**

322 During phase separations, macromolecules partition into distinct biochemical
323 compartments characterized by a higher concentration dense phase and a lower concentration
324 dilute phase (23, 24, 26). The dense compartment can have either liquid-like properties in liquid-
325 to-liquid phase separations or solid-like properties in liquid-to-solid phase transitions (24, 25, 27,
326 47). To determine whether TIR undergoes a liquid-to-liquid or a liquid-to-solid phase transition,
327 we assayed the enzyme activity of TIR in the presence of 1,6-hexanediol, an aliphatic alcohol that
328 interferes with hydrophobic interactions prominent in liquid-to-liquid separations. Thus, 1,6-
329 hexanediol disrupts liquid-like compartments, but not solid-like compartments (23, 26, 27). In the
330 presence of either PEG 3350 or citrate, we observed that 1,6-hexanediol decreases the NADase
331 activity of TIR by <2-fold, yet the activity of 1,6-hexanediol-treated TIR remains two orders of
332 magnitude higher than the activity of TIR without PEG 3550 or citrate addition (Fig. 5*A*). While
333 significant, this modest effect suggests that the NADase activity of TIR is predominantly
334 associated with a solid, rather than a liquid, state (Fig. 5*A*). Notably, in the absence of PEG 3350
335 or citrate, the low-level TIR NADase activity can be inhibited by 1,6-hexanediol (Fig. 5*A*),
336 suggesting that this activity is driven by hydrophobic interactions. Importantly, 1,6-hexanediol
337 does not interfere with TIR precipitation in the presence of PEG or citrate, regardless of whether
338 it is added before or after precipitate formation (Fig. S5*A* and *B*).

339 Next, we determined if this liquid-to-solid phase transition of TIR is reversible. The
340 insoluble fraction following treatment of TIR with PEG 3350 or citrate was resuspended in either
341 buffer alone or buffer plus the respective additive (PEG 3350 or citrate). If the phase transition is
342 reversible, resuspension of precipitated TIR in buffer alone should disrupt enzymatic activity.

343 However, if the phase transition is irreversible, activity should be detected when the pellet is
344 resuspended in buffer alone. Notably, we observed some TIR enzymatic activity when the pellet
345 was resuspended in buffer (Fig. 5*B*). With PEG 3350, the activity was lower than that observed in
346 the pre-centrifugation control or when the pellet was resuspended in buffer with PEG 3350. By
347 contrast, with citrate, the activity was similar to both control conditions (pre-centrifugation or when
348 the pellet was resuspended in buffer and citrate). These data indicate that the phase transition of
349 TIR is partially reversible in PEG 3350 and irreversible in sodium citrate. To confirm these findings,
350 we centrifuged the resuspended samples to examine the fractions visually by SDS-PAGE. In the
351 sample initially prepared with PEG 3350 and resuspended in buffer alone, a faint band was
352 present in the supernatant fraction. However, this band was absent in the sample initially prepared
353 with sodium citrate (Fig. 5*C*). These data confirm that the TIR phase transition is partially
354 reversible in PEG 3350 and irreversible in sodium citrate, at least under these conditions.

355 Next, we evaluated the effect of pH on TIR precipitation and NADase activity. There was
356 virtually no increase in TIR precipitation in the absence of PEG. However, in the presence of 25%
357 PEG, TIR precipitation increased with increasing pH (Fig. 5*D*). Under these same conditions, no
358 activity was apparent below pH 6. K_m remained constant (Fig. 5*E*) and k_{cat} increased from pH 6.5
359 to pH 8.5 (Fig. 5*F*). A corresponding increase in k_{cat}/K_m was responsible for the increase in
360 catalytic efficiency above pH 7 (Fig. 5*G*). Notably, the increase in k_{cat}/K_m correlated with
361 precipitation (Fig. 5*D* and *G*), again indicating that a phase transition increases TIR activity.

362 We performed negative stain electron microscopy to directly visualize TIR aggregation *in*
363 *vitro*. Protein visualization is not possible with PEG because macroviscogens themselves are
364 stained, confounding image analysis. Therefore, we performed this experiment with citrate. In the
365 absence of citrate, we observed borderline fibrillar structures and protein aggregates, but overall,
366 there were no consistent structures (Fig. 5*H*). In the presence of citrate, however, circular particles
367 emerged (Fig. 5*I*). These results indicate that, *in vitro*, TIR aggregates into higher-order, ring-like
368 structures.

369 Taken together, these data demonstrate that the TIR domain undergoes a phase
370 transition, which superactivates its NADase activity to initiate the p38 PMK-1 innate immune
371 pathway.
372
373 **Sterol scarcity primes p38 PMK-1 immune defenses.**
374 *C. elegans* require cholesterol to survive bacterial infection. However, nematodes lack the
375 ability to synthesize cholesterol *de novo*, and therefore must obtain this essential metabolite from
376 their diet. Thus, we hypothesized that, when environmental sterols are limited, activation of the
377 p38 PMK-1 pathway represents an evolutionary adaptation that primes immune effector
378 expression to anticipate challenges from bacterial pathogens. To test this hypothesis, we
379 examined the expression of innate immune effector genes during bacterial infection in the
380 presence and absence of cholesterol supplementation. Interestingly, the induction of *irg-4*p::*gfp*
381 (Fig. 6*A*), *irg-5*p::*gfp* (Fig. 6*B*) and T24B8.5p::*gfp* (Fig. 6*C*) during *P. aeruginosa* infection was
382 enhanced when nematodes were infected on media that did not contain supplemented
383 cholesterol. Consistent with these data, *P. aeruginosa* infection also led to increased activation of
384 *irg-4*p::*gfp* (Fig. 6*D*) and *irg-5*p::*gfp* (Fig. 6*E*) when *nhr-8* was depleted by RNAi. These data
385 suggest that cholesterol scarcity primes p38 PMK-1 immune defenses for subsequent pathogen
386 encounter.
387 To provide further support for this hypothesis, we analyzed the expression pattern of p38
388 PMK-1-dependent transcripts in *nhr-8(hd117)* mutant animals during *P. aeruginosa* infection. Of
389 the 472 genes that were induced in wild-type animals during *P. aeruginosa* infection, 184 were
390 also differentially regulated (either induced or repressed) in *nhr-8(hd117)* animals that were
391 infected with *P. aeruginosa*. To perform this analysis in an unbiased manner, we scaled the
392 expression level in each condition for each of these 184 genes by calculating a row z-score and
393 performed hierarchical clustering (Fig. 6*F*). We observed that these 184 genes group into two
394 clusters: Cluster I had 139 genes and Cluster II contained 45 genes (Table S3). Cluster I was

395 comprised mostly of genes whose expression in the absence of infection was higher in *nhr-*
396 *8(hd117)* mutants than wild-type animals (129 of 139 genes). In addition, the majority of Cluster I
397 genes were more strongly induced during *P. aeruginosa* infection in *nhr-8(hd117)* animals than
398 wild-type animals. Cluster II, on the other hand, contained genes whose induction on *P.*
399 *aeruginosa* were dependent on *nhr-8*. Interestingly, p38 PMK-1-dependent genes were strongly
400 enriched among Cluster I, but not Cluster II, genes (Fig. 6*G*). Thirty-three of the 139 genes in
401 Cluster I are known targets of the p38 PMK-1 immune pathway (24.17-fold enriched,
402 hypergeometric p-value = 7.68×10^{-37}), a group that includes the immune effectors T24B8.5 (Fig.
403 6*H*), *irg-4* (Fig. 6*I*), *irg-5* (Fig. 6*J*) and K08D8.4 (Fig. 6*K*). By contrast, only three genes in Cluster
404 II are p38 PMK-1 dependent transcripts (6.95-fold enriched, hypergeometric p-value = 0.01) (Fig.
405 6*F* and 6*G*).

406 These data demonstrate that sterol scarcity primes the induction of innate immune
407 effectors by activating the p38 PMK-1 immune pathway (Fig. 6*L*). Subsequent challenge by *P.*
408 *aeruginosa* further drives immune activation in a manner that promotes clearance of pathogenic
409 bacteria from the intestine (Fig. 1*N*).

410 **DISCUSSION**

411 Here, we show that the nematode *C. elegans* adapts to a sterol-deficient environment by
412 activating immune defenses in the intestine via the p38 PMK-1 pathway. In the absence of dietary
413 cholesterol, *C. elegans* are more susceptible to infection with pathogenic bacteria and have a
414 shortened lifespan (6, 7, 13). In addition, sterol scarce environments prime some *C. elegans*
415 larvae to enter dauer diapause, an alternative, stress-resistant growth form. We show that
416 anticipatory activation of the p38 PMK-1 pathway during conditions of low sterol availability is an
417 adaptive response in animals that do not enter dauer diapause.

418 In this study, we also define the mechanism of p38 PMK-1 immune pathway activation in
419 *C. elegans*. We show that TIR-1/SARM1 undergoes a phase transition to potentiate its intrinsic
420 NAD^+ glycohydrolase activity and activate innate immune defenses in intestinal epithelial cells via
421 the p38 PMK-1 pathway. Accordingly, activation of the p38 PMK-1 pathway when dietary sterols
422 are limited requires TIR-1/SARM1 multimerization and precipitation.

423 The p38 PMK-1 pathway controls the expression of innate immune effector genes. Inputs
424 from chemosensory neurons, bacterial density, tissue damage and nucleotide metabolism also
425 regulate the tonic level of p38 PMK-1 pathway activity (16, 48-52). These data suggest that p38
426 PMK-1 phosphorylation is adjusted in different environments to anticipate dangerous threats
427 during periods of vulnerability. Consistent with this hypothesis, the increased level of p38 PMK-1
428 phosphorylation during sterol deprivation leads to enhanced activation of immune effector genes
429 and promoted pathogen clearance from the intestine during a subsequent bacterial infection.

430 We previously demonstrated that a *C. elegans* nuclear hormone receptor, NHR-86, a
431 member of a family of ligand-gated transcription factors, surveys the chemical environment to
432 activate the expression of immune effectors (32). Interestingly, NHR-86 targets immune effectors
433 whose basal regulation requires the p38 PMK-1 immune pathway. However, NHR-86 functions
434 independently of PMK-1 and modulates the transcription of these infection response genes
435 directly. NHR-86 is a nematode homolog of the mammalian nuclear hormone receptor hepatocyte

436 nuclear factor 4 (HNF4), a family of NHRs that expanded dramatically in *C. elegans* — 259 HNF4
437 homologs are encoded in the *C. elegans* genome (53, 54). One potentially unifying hypothesis is
438 that HNF4 homologs detect pathogen- or host-derived ligands that are associated with infection
439 and activate pathogen-specific immune defenses. In this model, the p38 PMK-1 pathway
440 functions as a rheostat that receives inputs from signals associated with potentially dangerous
441 environmental conditions to prime host immune effector genes. Thus, upon encountering a
442 pathogen, immune defenses can be further augmented by mechanisms that detect pathogen
443 specifically.

444 Intracellular signaling is coordinated through the formation of membrane-less, phase-
445 separated compartments that concentrate signaling components and mediators to facilitate rapid
446 cellular responses (20-22, 24, 47). In a contemporaneous study, we uncovered that the phase
447 transition of the mammalian homolog of TIR-1, SARM1, also potentiates its intrinsic NADase
448 activity (55). Consistent with the data presented in this manuscript, mammalian SARM1 with
449 mutations in residues required for multimerization largely failed to undergo a phase transition and
450 lack NADase catalytic activity. SARM1 has a well-characterized role in promoting Wallerian
451 degeneration, a form of neuronal degeneration induced by axon injury (56, 57). During axon injury,
452 SARM1 NADase activity depletes NAD^+ and induces cell death, through a non-canonical cell
453 death pathway (58). Additionally, in myeloid cells, SARM1 localizes to mitochondria and causes
454 mitochondrial depolarization and cell death during inflammasome activation (59). Thus, the
455 regulation of intracellular signaling activity through phase transition of TIR-1/SARM1 and its NAD^+
456 glycohydrolase activity is evolutionarily ancient and is essential for diverse physiological
457 processes, including neuronal degeneration, cell death, and innate immune regulation in the
458 intestine.

ACKNOWLEDGEMENTS AND FUNDING SOURCES

The authors thank Alexandra Byrne, Victoria Czech, Lauren O'Connor, and Heather Loring for helpful discussions. The authors are also grateful to Melanie Trombly and Merin MacDonald for critical reading of the manuscript. This research was supported by R01 AI130289 (to R.P.W.), R21 AI163430 (to R.P.W.), an Innovator Award from the Kenneth Rainin Foundation (to R.P.W.), the Dan and Diane Riccio Fund for Neuroscience (to R.P.W. and P.R.T.), F30 AI150127 (to N.D.P.), T32 AI132152 (to N.D.P. and J.D.I.), T32 GM107000 (to N.D.P.), and R35 GM118112 (to P.R.T.). Some strains were provided by the *Caenorhabditis* Genetics Center, which is funded by the NIH Office of Research Infrastructure Programs (P40 OD010440).

468 **MATERIALS AND METHODS**

469 ***C. elegans* and bacterial strains.** The previously published *C. elegans* strains used in this
470 study were: N2 Bristol (28), KU25 *pmk-1(km25)* (60), AU3 *nsy-1(ag3)* (14), ZD101 *tir-1(qd4)*
471 (29), AA968 *nhr-8(hd117)* (13), AE501 *nhr-8(ok186)* (31), AU78 *agIs219* [T24B8.5p::*gfp*::*unc-*
472 *54*-3'UTR; *ttx-3*p::*gfp*::*unc-54*-3'UTR] (29), AU306 *agIs44* [*irg-4*p::*gfp*::*unc-54*-3'UTR*; myo-*
473 *2*p::*mCherry*] (61), AY101 *acIs101* [p*DB09.1(irg-5*p::*gfp)*; pRF4(*rol-6(su1006)*)] (30), TJ356
474 *zIs356* [*daf-16*p::*daf-16a/b*::*gfp* + pRF4(*rol-6(su1006)*)], *MGH167 sid-1(qt9); alxIs9[vha-6p::sid-*
475 *1::SL2::GFP]*. The strains developed in this study were: RPW278 *nhr-8(hd117)*;*agIs219*,
476 RPW317 *tir-1(qd4)*;*nhr-8(hd117)*, RPW280 *nhr-8(hd117)*;*umsEx42*[*nhr-8*p::*nhr-8*::3'-UTR*; myo-*
477 *2*p::*mCherry*), RPW281 *nhr-8(hd117)*;*umsEx43*[*nhr-8*p::*nhr-8*::3'-UTR*; myo-2*p::*mCherry*),
478 RPW288 *nhr-8(hd117)*;*umsEx50*[*ges-1*p::*nhr-8*::3'-UTR*; myo-2*p::*mCherry*), RPW289
479 *umsEx51*[*ges-1*p::*nhr-8*::3'-UTR*; myo-2*p::*mCherry*), RPW290 *umsEx52*[*ges-1*p::*nhr-8*::3'-UTR*;*
480 *myo-2*p::*mCherry*), RPW284 *nhr-8(hd117)*;*umsEx46*[*sng-1*p::*nhr-8*::3'-UTR*; myo-2*p::*mCherry*),
481 RPW286 *nhr-8(hd117)*;*umsEx48*[*sng-1*p::*nhr-8*::3'-UTR*; myo-2*p::*mCherry*), RPW287 *nhr-*
482 *8(hd117)*;*umsEx49*[*sng-1*p::*nhr-8*::3'-UTR*; myo-2*p::*mCherry*). RPW339 *tir-*
483 *1(ums47[E788A])*;*agIs219*, RPW369 *tir-1(ums54[ΔSAM])*;*agIs219*, RPW374 *tir-*
484 *1(ums55[G747P])*;*agIs219*, RPW381 *tir-1(ums56[H833A])*;*agIs219*, RPW386 *tir-1(ums57[tir-*
485 *1::3xFLAG])*;*agIs219*, RPW387 *tir-1(ums58[tir-1[E788A]::3xFLAG])*;*agIs219*, RPW388 *tir-1*
486 *(ums59[tir-1[ΔSAM]::3xFLAG])*;*agIs219*, RPW 389 *tir-1(ums60[tir-1[G747P]::3xFLAG])*;*agIs219*.
487 Bacteria used in this study are *Escherichia coli* OP50, *E. coli* DH5α, *E. coli* HT115(DE3), and
488 *Pseudomonas aeruginosa* strain PA14 (62).

489

490 ***C. elegans* growth conditions and lipid supplementation.** *C. elegans* strains were maintained
491 on standard nematode growth medium (NGM) plates [0.25% bacto peptone, 0.3% sodium
492 chloride, 1.7% agar, 5 µg/mL cholesterol (Sigma-Aldrich, BioReagent grade), 25 mM potassium
493 phosphate pH 6.0, 1 mM magnesium sulfate, 1 mM calcium chloride] with *E. coli* OP50 as a food

494 source, as described (28). For low cholesterol medium (0 µg/mL cholesterol), NGM was prepared
495 without cholesterol supplementation, while 0.1% ethanol added to maintain an equivalent ethanol
496 concentration. For high cholesterol medium, cholesterol was dissolved in ethanol at 20 mg/mL
497 and added to NGM at a final concentration of 80 µg/mL immediately prior to pouring plates. For
498 all assays with high cholesterol medium, control NGM containing 0.4% ethanol and 5 µg/mL
499 cholesterol were used as control plates. Cholesterol solubilization assays were performed by
500 supplementing NGM containing 5 µg/mL cholesterol with either 0.1% Tergitol (Sigma-Aldrich) or
501 0.1% Triton X-100 (Sigma-Aldrich). For assays using media solidified with agarose, NGM plates
502 were prepared with 1.7% Ultrapure agarose (ThermoFisher Scientific) in place of agar. All fatty
503 acids were purchased from Nu-Check-Prep Inc. and supplementation performed as previously
504 described with modification (63, 64). Fatty acids were dissolved in 50% ethanol and added at a
505 final concentration of 1 mM to NGM agarose containing 0 µg/mL cholesterol and 0.1% Tergitol
506 immediately prior to plate pouring. Prior to all assays, plates supplemented with lipids and control
507 plates were seeded with *E. coli* OP50 and grown for 24 hours at room temperature. Assays were
508 performed by picking 10-20 gravid adult animals to either lipid supplemented or matched control
509 plates. Animals were maintained on the plates for 14 hours at 20ºC after which they were
510 removed. Eggs laid on the plate were allowed to hatch and develop to the L4 stage at 20ºC. For
511 low cholesterol assays, animals were grown for two generations on NGM containing 0 µg/mL
512 cholesterol.
513
514 ***C. elegans* strain construction**. CRISPR/Cas9 was used to generate *tir-1* mutants in both wild-
515 type and TIR-1::3xFLAG backgrounds, as described (65, 66). All CRISPR/Cas9 reagents were
516 purchased from Integrated DNA Technologies. Target guide sequences were selected using the
517 CHOPCHOP web tool (67). ssODN repair templates contained indicated edits, deletions or
518 insertions with 35 bp flanking homology arms. crRNA guide and ssODN sequences are listed in
519 Table S4. A mixture of 0.25 µg/µL Cas9, 0.1 µg/µL tracrRNA and 0.056 µg/µL crRNA were

520 incubated for 15 minutes at 37ºC. 0.11 µg/µL ssODN and 40 ng/µL pRF4(*rol-6(su1006)*) plasmid
521 were added to the mixture, centrifuged and microinjected into young adult animals carrying the
522 *agIs219* transgene or *tir-1(ums57[tir-1::3xFLAG])*;*agIs219*. The F1 progeny were screened for Rol
523 phenotypes 3-4 days after injection and then for indicated edits using PCR and Sanger
524 sequencing. Primer sequences used for genotyping are listed in Table S4.
525
526 **Feeding RNAi.** Knockdown of target genes was performed by feeding *C. elegans E. coli* HT115
527 expressing dsRNA targeting the gene of interest, as previously described with modification (68-
528 70). In brief, HT115 bacteria expressing dsRNA targeting genes of interest were grown in
529 Lysogeny broth (LB) Lennox medium containing 50 µg/mL ampicillin and 15 µg/mL tetracycline
530 overnight with shaking (250 rpm) at 37ºC. Overnight cultures were seeded onto NGM containing
531 5 mM IPTG and 50 µg/mL carbenicillin and incubated at 37ºC for 16 hours after which
532 synchronized L1 animals were transferred to bacterial lawns and allowed to grow until the L4
533 stage.
534
535 ***C. elegans* Bacterial Infection and Colonization Assays.** "Slow killing" *P. aeruginosa* infection
536 experiments were performed as previously described (71, 72). Wild-type is either N2 or *agIs219*.
537 In brief, a single colony of *P. aeruginosa* PA14 was inoculated into 3-mL of LB medium and grown
538 with shaking (250 rpm) at 37ºC for 14 hours. 10-µL of overnight culture was spread onto 35-mm
539 petri dishes containing 4-mL slow killing agar (0.35% peptone, 0.3% sodium chloride, 1.7% agar,
540 5 µg/mL cholesterol, 25 mM potassium phosphate pH 6.0, 1 mM magnesium sulfate, 1 mM
541 calcium chloride). Plates were incubated for 24 hours at 37ºC and for approximately 24 hours at
542 25ºC. Immediately prior to starting the assay 0.1 mg/mL 5-fluorodeoxyuridine (FUDR) was added
543 on top of the agar to prevent progeny from hatching. Animals used in all assays were grown at
544 20ºC with specified growth conditions. For assays involving high cholesterol or nonionic
545 detergents, slow killing agar plates were prepared with either 80 µg/mL cholesterol (Sigma-

546 Aldrich), 0.1% Tergitol (Sigma-Aldrich), or 0.1% Triton X-100 (Sigma-Aldrich). For experiments
547 using plates containing 80 µg/mL cholesterol, matched control plates containing the equivalent
548 ethanol concentration (0.4%) and 5 µg/mL cholesterol were prepared. All pathogenesis and
549 lifespan assays are representative of three biological replicates. Sample sizes, mean lifespan,
550 and p values for all trials are shown in Table S2.

551 Colony forming units of *P. aeruginosa* were quantified in the intestine of *C. elegans* as
552 previously described with modifications (73, 74). Briefly, *C. elegans* animals were exposed to
553 lawns of *P. aeruginosa*, which were prepared as previously described, for 24 hours. Animals were
554 then picked to NGM plates lacking bacteria and incubated for 10 minutes to remove external *P.*
555 *aeruginosa*. Animals were then transferred to a second NGM plate after which 10-11 animals per
556 replicate were collected, washed with M9 buffer containing 25 mM tetramisole (Sigma-Aldrich)
557 and 0.01% Triton X-100 (Sigma-Aldrich), and ground with 1.0 mm silicon carbide beads (BioSpec
558 Products). *P. aeruginosa* CFUs were quantified from serial dilutions of the lysate grown on LB
559 agar.

560

561 **Gene expression analysis and bioinformatics.** Synchronized L1 stage *C. elegans* of the
562 indicated genotypes were grown to the L4 stage and harvested by washing with M9. For
563 expression analysis of *C. elegans* genes during *P. aeruginosa* infection, animals at the L4 stage
564 animals were transferred by washing to plates containing *E. coli* OP50 or *P. aeruginosa* PA14
565 lawns. Animals were exposed for four hours and subsequently harvested by washing with M9.
566 RNA was isolated using TriReagent (Sigma-Aldrich), column purified (Qiagen), and analyzed by
567 100 bp paired-end mRNA-sequencing using the BGISEQ-500 platform (BGIAmericasCorp) with
568 >20 million reads per sample. Raw fastq reads were evaluated by FastQC (version 0.11.5), clean
569 reads were aligned to the *C. elegans* reference genome (WBcel235) and quantified using Kallisto
570 (version 0.45.0) (75). Differentially expressed genes were identified using Sleuth (version 0.30.0)
571 (76). Pearson correlation statistical analysis was performed using Prism 9.0. Heat-maps of

572 differentially expressed genes were generated using pheatmap (version 1.0.12). Gene set
573 enrichment analysis of RNA-seq was performed using GSEA (version 4.1.0) (77) with a custom
574 gene set database containing p38 PMK-1 dependent genes generated from previously published
575 RNA-seq of uninfected *pmk-1(km25)* animals (78). Differential gene expression was defined as a
576 fold change (FC) versus wild-type greater than 2 and q less than 0.01.

577 For the qRT-PCR studies, RNA was reverse transcribed to cDNA using the iScript™ cDNA
578 Synthesis Kit (Bio-Rad Laboratories, Inc.), amplified and detected using Syber Green (Bio-Rad
579 Laboratories, Inc.) and a CFX384 machine (Bio-Rad Laboratories, Inc.). The sequences of
580 primers that were designed for this study are presented in Table S4. Other primers were
581 previously published (17, 79-81). All values were normalized against the geometric mean of the
582 control genes *snb-1* and *act-3*. Fold change was calculated using the Pfaffl method (82).

583

584 **Immunoblot analyses.** Protein lysates from *C. elegans* grown to the L4 larval stage on *E. coli*
585 OP50 on NGM agar were prepared as previously described with modification (32, 83). Harvested
586 animals were washed twice with M9 buffer and resuspended in RIPA Buffer (Cell Signaling
587 Technology, Inc.) containing 1x Halt Protease and Phosphatase inhibitor (ThermoFisher
588 Scientific). Samples were lysed using a teflon homogenizer, centrifuged, and protein was
589 quantified from the supernatant of each sample using the DC protein assay (Bio-Rad
590 Laboratories, Inc.). NuPAGE™ LDS sample buffer (ThermoFisher Scientific) was added to a
591 concentration of 1X and 12.5-30 µg of total protein from each sample was resolved on NuPAGE™
592 4-12% BisTris (Phospho-PMK-1 and Total-PMK-1) or NuPAGE™ 3-8% TrisAcetate (TIR-
593 1::3xFLAG) gels (ThermoFisher Scientific), transferred to nitrocellulose membranes using a
594 Trans-Blot Turbo Transfer System (Bio-Rad Laboratories, Inc.), blocked with 5% milk powder in
595 TBST and probed with a 1:1000 dilution of an antibody that recognizes the doubly-phosphorylated
596 TGY motif of PMK-1 (Cell Signaling Technology, #9211), a previously characterized total PMK-1
597 antibody (32), a monoclonal mouse anti-FLAG antibody (Sigma-Aldrich, M2), or a monoclonal

598 mouse anti-tubulin antibody (Sigma-Aldrich, Clone B-5-1-2). Horseradish peroxidase (HRP)-
599 conjugated anti-rabbit (Cell Signaling Technology, #7074) and anti-mouse IgG secondary
600 antibodies (Abcam, #ab6789) were diluted 1:10,000 and used to detect the primary antibodies
601 following the addition of ECL reagents (Thermo Fisher Scientific, Inc.), which were visualized
602 using a BioRad ChemiDoc MP Imaging System. The band intensities were quantified using
603 ImageJ version 2.0.0, and the ratio of active phosphorylated PMK-1 to total PMK-1 was
604 calculated.
605
606 **Generation of transgenic *C. elegans* strains.** To generate *nhr-8* rescue lines, 1989 bp of the
607 *nhr-8* promoter region upstream of the 5'-UTR, and the entire *nhr-8* coding region, including the
608 5'-UTR and 3'-UTR were amplified and PCR purified. Gibson assembly was used to clone PCR
609 products into a *Sma*I-linearized pUC19 vector. Plasmids were transformed into chemically
610 competent *E. coli* DH5α and selected on LB agar with 50 µg/mL ampicillin. For tissue specific
611 rescue of *nhr-8* expression, 1973 bp of *sng-1* promoter region (neuronal specific expression),
612 1936 of *ges-1* promoter region (intestinal specific expression) and the *nhr-8* coding region were
613 PCR amplified, purified and cloned into a *Sma*I-linearized pUC19 vector by Gibson assembly,
614 transformed into chemically competent *E. coli* DH5α, and selected on LB agar with 50 µg/mL
615 ampicillin. All plasmids were verified by Sanger sequencing. Primer sequences used for cloning
616 are listed in Table S4. Plasmids (50 ng/µL), the *myo-2*p::*mCherry* co-injection marker (5 ng/µL)
617 and pUC19 vector (155 ng/µL) were microinjected into *nhr-8(hd117)* animals to generate the
618 arrays for native expression (*umsEx42*, *umsEx43*), intestinal specific expression (*umsEx50*,
619 *umsEx51*, *umsEx52*), and neuronal specific expression (*umsEx46*, *umsEx48*, *umsEx49*).
620
621 **Microscopy.** Nematodes were mounted onto agar pads, paralyzed with 10 mM levamisole
622 (Sigma) and photographed using a Zeiss AXIO Imager Z2 microscope with a Zeiss Axiocam

623 506mono camera and Zen 2.3 (Zeiss) software.

624

625 **TIR-1 TIR domain expression and purification.** The recombinant *C. elegans* TIR-1 TIR domain
626 (TIR) was expressed in bacteria as previously described (55). Briefly, the TIR domain cloned into
627 the pET-30a(+) vector was transformed into chemically competent *E. coli* BL21(DE3) cells and
628 maintained as a glycerol stock at -80 °C. An inoculation loop was used to transfer the transformed
629 bacteria into 5-mL of LB media with 50 µg/mL (final concentration) of kanamycin and the culture
630 was grown overnight at 37 °C while rotating. The next day, the cultures were diluted 1:400 in LB
631 media with 50 µg/mL (final concentration) of kanamycin and grown at 37 °C while shaking at 215
632 rpm until an OD_{600} of 0.7-0.8 was reached. After cooling, 50 µM IPTG (final concentration) was
633 added to the culture to induce protein expression. The incubator temperature was decreased to
634 16 °C and cells were incubated for an additional 16-18 h. Bacterial cells were collected by
635 centrifugation at 3,000 *x g* for 15 min at 4 °C, flash frozen in liquid nitrogen, and stored at -80 °C
636 until purification.

637 For purification, bacterial pellets were thawed on ice and then resuspended in Lysis Buffer
638 (50 mM Tris•HCl pH 7.0, 300 mM NaCl, 10% (w/v) glycerol, 0.001% Tween 20) with Pierce™
639 EDTA-free protease inhibitor mini tablets (ThermoFisher Scientific). The resuspension was
640 incubated with 100 µg/mL lysozyme for 10 min at 4 °C and sonicated with a Fisher Scientific Sonic
641 Dismembrator sonicator (FB-705) in 50-mL batches at an amplitude of 30 for 20 s, pulsing for 1 s
642 on and 1 s off, followed by a delay period of 20 s for a series of 12 cycles. Crude lysate was
643 clarified at 21,000 *x g* for 25 min at 4 °C, at which point the supernatant was applied to pre-
644 equilibrated Strep-Tactin XT Superflow high-capacity resin (IBA Lifesciences) and allowed to
645 enter the column by gravity flow; the Strep-Tactin resin had been equilibrated in Strep Wash
646 Buffer (50 mM Tris•HCl pH 7.0, 300 mM NaCl). The column was washed with 30 column volumes
647 of Strep Wash Buffer and the protein was eluted with 25 column volumes of Strep Elution Buffer
648 (Strep Wash Buffer with 50 mM biotin). Protein eluted from the Strep-Tactin column was then

649 applied to pre-equilibrated TALON Metal Affinity Resin (Takara) and allowed to enter the column
650 by gravity flow; the TALON resin was equilibrated in His Wash 1 (50 mM Tris•HCl pH 7.0, 150
651 mM NaCl, 5 mM imidazole). A series of 15 column volume washes were applied (His Wash 1; His
652 Wash 2: 50 mM Tris•HCl pH 7.0, 150 NaCl, 10 mM imidazole) and the protein was eluted in 20
653 column volumes of His Elution Buffer (50 mM Tris•HCl pH 7.0, 150 mM NaCl, 150 mM imidazole).
654 The eluted protein was dialyzed overnight in Dialysis Buffer (50 mM Tris•HCl, pH 7.0, 150 mM
655 NaCl). The next day, the protein was concentrated using a 10,000 NMWL Amicon Ultra-15
656 Centrifugal Filter Unit at 4 °C and the protein concentration was determined by the Bradford
657 assay. TIR was flash frozen in liquid nitrogen and stored at -80 °C in 25-μL aliquots.
658
659 **Fluorescent NADase Assay.** Nicotinamide 1,N^6-ethenoadenine dinucleotide (ε-NAD, Sigma-
660 Aldrich) is a fluorescent analog of NAD^+ and was utilized in kinetic assays as a TIR-1 substrate.
661 TIR-1 cleaves the nicotinamide moiety from ε-NAD to release nicotinamide and etheno-ADPR (ε-
662 ADPR), which fluoresces (λ_{ex} = 330 nm, λ_{em} = 405 nm). Enzymatic activity was assayed in Assay
663 Buffer (50 mM Tris pH 8.0, 150 mM NaCl; final concentration) using Corning® 96–well Half Area
664 Black Flat Bottom Polystyrene NBS™ Microplates for a final reaction volume of 60-μL, or
665 Corning® 384-well Low Volume Black Round Bottom Polystyrene NBS™ Microplates for a final
666 volume of 20-μL; reactions were initiated by the addition of ε-NAD. ε-ADPR fluorescence intensity
667 readings were taken in real time every 15 s for 15-30 min using Wallac EnVision Manager
668 software and a PerkinElmer EnVision 2104 Multilabel Reader. Fluorescence intensity readings
669 (λ_{ex} = 330 nm, λ_{em} = 405 nm) were converted to [ε-ADPR] with an ε-ADPR standard curve, which
670 was produced by incubating fixed concentrations (0-400 μM) of ε-NAD with excess ADP-ribosyl
671 cyclase and plotting the peak fluorescence intensity values against [ε-ADPR]. The activity was
672 linear with respect to time under all conditions tested.
673

674 **Effect of crowding agents and sodium citrate on the activity of the TIR domain.** The
675 enzymatic activity of the TIR domain was evaluated using the Fluorescent Assay described
676 above. First, the enzyme concentration dependence was determined. For purified protein, the
677 enzyme (0-32.5 μM; final concentration) was added to Assay Buffer in duplicate, briefly incubated
678 at room temperature for 10 min, and the reaction was initiated with 1 mM ε-NAD. Fluorescence
679 intensity was monitored in real time every 15 s for 15 min.

680 To evaluate the effect of crowding agents and sodium citrate on TIR activity, stock
681 solutions of the additives were made. 50% (w/v) solutions of PEGs 8000, 3500, 1500, and 400,
682 as well as 60% (w/v) solutions of dextran, sucrose, and glycerol were prepared and filtered.
683 Initially, the concentration dependence of TIR in the presence of PEG 3350 was determined. TIR
684 (0-15 μM; final concentration) was added to Assay Buffer with 25% PEG 3350 (final concentration)
685 in duplicate, incubated for 10 min at room temperature, initiated with 1 mM ε-NAD, and monitored
686 every 15 s for 15 min. The concentration dependence of TIR in 25% PEG 3350 was used to
687 establish that 2.5 μM TIR could be used to enable robust kinetic analyses. Next, the effect of
688 viscogens on TIR activity was evaluated by adding 2.5 μM TIR (final concentration) in duplicate
689 to Assay Buffer with or without 25% w/v of the viscogens (final concentration). Following a brief
690 10 min incubation period, the reaction was initiated with 1 mM ε-NAD and monitored every 15 s
691 for 20 min. The dose response of 2.5 μM TIR to the viscogens (0, 10, 20, and 30% final
692 concentrations) was evaluated in the same manner and monitored every 15 s for 15 min.

693 Sodium citrate was prepared as a stock solution of 2 M and filtered. The concentration
694 dependence of TIR in the presence of 500 mM sodium citrate was determined. TIR (0-15 μM;
695 final concentration) was added to Assay Buffer with 500 mM citrate (final concentration) in
696 duplicate, incubated for 10 min at room temperature, and then the reaction was initiated with 1
697 mM ε-NAD and monitored every 15 s for 15 min. Additionally, the dose dependence of sodium
698 citrate was determined in duplicate. 2.5 μM TIR was added to Assay Buffer with (0-1000 mM)

699 sodium citrate and briefly incubated at room temperature for 10 min. The reaction was initiated
700 with 1 mM E-NAD, and fluorescence was monitored for 15 min every 15 s.
701 In all cases, the fluorescence intensity was converted to ε-ADPR using the ε-ADPR
702 standard curve described above. Slopes of the progress curves yielded the velocities of the
703 reactions, which were plotted in GraphPad Prism.
704
705 **Effect of PEG 3350 and sodium citrate on steady state kinetics.** Steady state kinetic reactions
706 were carried out in Assay buffer with either PEG 3350 (0-25%; final concentration) or sodium
707 citrate (0-1000 mM; final concentration); a constant concentration of 2.5 μM TIR was used in these
708 assays. Reaction components were mixed in duplicate and incubated at room temperature for 10
709 min before initiating the reaction with ε-NAD (0-4000 μM, final concentration). Fluorescence
710 intensity was monitored for 15 min every 15 s. Using the ε-ADPR standard curve, the fluorescence
711 was converted to [ε-ADPR]. The velocity of the reactions was calculated from the slope of the
712 progress curve at each ε-NAD concentration and plotted in GraphPad Prism. Kinetic parameters
713 were determined by fitting these velocities to the Michaelis Menten equation (Eq. 1) at each PEG
714 3350 or sodium citrate concentration. K_m, k_{cat}, and k_{cat}/K_m values were plotted against PEG 3350
715 or sodium citrate concentration.
716 Eq.1 $v = \frac{V_{max}[S]}{K_m+[S]}$,
717 Where V_{max} is the maximum velocity, [S] is the substrate concentration, and K_m is the substrate
718 concentration at half the maximum velocity.
719
720 **The TIR domain precipitates in PEG3350 and sodium citrate.** 5 μM TIR was incubated in
721 Assay Buffer with PEG 3350 (0, 10, 17.5, and 25%; final concentration) or sodium citrate (0, 125,
722 250, 500, 750, and 1000 mM; final concentration) in duplicate at room temperature for 15 min.
723 The precentrifugation control was removed and the remainder of the sample was centrifuged at

724 17,000 *x g* at 4 °C for 10 min. Following centrifugation, the supernatant was separated from the
725 pellet and the pellet was resuspended in Assay Buffer with the respective concentration of PEG
726 3350 or sodium citrate. Samples were diluted 1:2 with gel loading buffer and run on an SDS-
727 PAGE gel. Protein bands were stained by Coomassie and visualized on a BioRad Gel Doc EZ
728 Gel Documentation System with Image Lab™ Software. Representative images are shown.
729 Following resuspension of the pellet, all fractions were analyzed in the Fluorescent Assay.
730 After the samples were aliquoted into the assay plate in duplicate, the enzymatic reaction was
731 initiated with 1 mM ε-NAD and monitored every 15 s for 15 min. Fluorescence intensity was
732 converted to ε-ADPR concentration using the ε-ADPR standard curve. Slopes of the progress
733 curves yielded the velocities of the reactions, which were plotted in GraphPad Prism.
734
735 **Effect of 1,6-hexanediol on TIR domain activity and precipitation.** To evaluate the effect of
736 1,6-hexanediol on TIR activity, the Fluorescent Assay was performed in triplicate in the absence
737 and presence of PEG 3350 or sodium citrate. For pure protein, 35 μM TIR (final concentration)
738 was incubated in Assay Buffer at room temperature for 10 min with or without 2% 1,6-hexanediol
739 (final concentration). For PEG 3350 or citrate, 2.5 μM TIR was incubated in Assay Buffer with
740 25% PEG 3350 or 500 mM sodium citrate (final concentrations) for 10 min at room temperature
741 with or without 2% 1,6-hexanediol. The reactions were initiated with 1 mM ε-NAD and monitored
742 for 15 min every 15 s. Using the ε-ADPR standard curve, fluorescence was converted to [ε-ADPR]
743 and the reaction velocities (i.e., slopes of the progress curves) obtained. Velocities were
744 normalized for enzyme concentration and these normalized velocities were plotted in GraphPad
745 Prism.
746 To determine whether 1,6-hexanediol can alter TIR precipitation, 1,6-hexanediol was
747 added either before or after TIR precipitation in duplicate. To assess whether 1,6-hexanediol
748 disrupts TIR precipitation, TIR precipitates were formed first by incubating 10 μM TIR (final
749 concentration) with 25% PEG3350 or 500 mM sodium citrate (final concentration) at room

750 temperature for 15 min. 1,6-hexanediol (0, 1, or 2%; final concentrations) was added to the
751 mixture and incubated at room temperature for an additional 10 min. The precentrifugation control
752 was removed and the remaining mixture was centrifuged at 21,000 *x g* for 10 min at 4 °C.
753 Supernatant fractions were removed, and the pellet was resuspended in Assay Buffer with the
754 respective additive and concentration of 1,6-hexanediol. All fractions were run on an SDS-PAGE
755 and stained with Coomassie Blue, and gels were imaged on a BioRad Gel Doc EZ Gel
756 Documentation System with Image Lab™ Software. Next, we determined if 1,6-hexanediol could
757 prevent TIR precipitation. 10 μM TIR was incubated in Assay Buffer with 1,6-hexanediol (0, 1, or
758 2 %; final concentration) for 15 min at room temperature. 25% PEG 3350 or 500 mM sodium
759 citrate was added to the TIR-buffer-hexanediol mixture and incubated further for 10 min. Controls
760 were removed and the samples were centrifuged at 21,000 *x g* for 10 min at 4 °C. As before,
761 supernatant fractions were removed, and pellet fractions were resuspended in Assay Buffer with
762 respective additives and hexanediol concentrations. Fractions were analyzed by SDS-
763 PAGE/Coomassie staining; representative images are shown.
764
765 **Phase Transition Reversibility.** To evaluate the reversibility of the TIR phase transition, 5 μM of
766 TIR was mixed with Assay Buffer and 25% PEG 3350 or 500 mM sodium citrate in duplicate (final
767 concentrations). Following a 15 min incubation period at room temperature, precentrifugation
768 controls were removed and the sample remaining was centrifuged at 17,000 *x g* for 10 min at 4
769 °C. Supernatant fractions were separated from the pellet, which was resuspended in either Assay
770 Buffer alone or Assay Buffer with respective additive. All fractions were analyzed for enzymatic
771 activity in the Fluorescent Assay. Briefly, the precentrifugation, supernatant, and pellet fractions
772 were aliquoted into the assay plates in duplicate and the reaction was initiated with 1 mM ε-NAD.
773 Fluorescence was converted to [ε-ADPR] concentration with the ε-ADPR curve to yield the
774 progress curves. The velocity of the reactions was taken as the slope of the line and the velocities
775 were plotted in GraphPad Prism.

776 To validate the kinetic data, 10 μM TIR (final concentration) was incubated in Assay Buffer
777 with either 25% PEG 3350 or 500 mM sodium citrate (final concentration) for 15 min at room
778 temperature; control samples were incubated in Assay Buffer only. Samples were centrifuged at
779 21,000 *x g* for 10 min at 4 °C, after which the supernatant was separated from the pellet. The
780 pellets from samples initially prepared with additives were resuspended in either Assay Buffer
781 alone or Assay Buffer plus the respective additive; this was not necessary for the sample initially
782 prepared without additive since the protein is primarily located in the supernatant in this case.
783 After removing another control sample (Additive lanes on gel), the resuspended samples were
784 centrifuged again at 21,000 *x g* for 10 min at 4 °C. As before, the supernatant was removed, and
785 the pellet was resuspended in Assay Buffer with the respective additive. All samples were
786 analyzed for protein content on an SDS-PAGE gel and stained with Coomassie Blue.
787
788 **Effect of pH on TIR domain precipitation and kinetics.** To determine the effect of pH on TIR
789 precipitation, the experiments described above were carried out in duplicate at pH values from
790 4.5-9.0. Briefly, 5 μM TIR (final concentration) was mixed with Assay Buffer (50 mM buffer; 150
791 NaCl) with and without 25% PEG 3350 (final concentration); for pH 4.5-5, sodium acetate buffer
792 was used; for pH 5.5-6.5, MES was used; for pH 7-9, Tris was used. The samples were incubated
793 for 15 min at ambient temperature, at which point the samples were centrifuged at 21,000 *x g* for
794 10 min at 4 °C. The supernatant was removed, and the pellet was resuspended in either buffer
795 alone or buffer with 25% PEG 3350 (final concentration); the presence or absence of 25% PEG
796 3350 and the buffer identity of the resuspension solution corresponded to the initial sample
797 preparation. 10-μL 1 M Tris, pH 6.8 was added to each sample to neutralize the buffer before
798 running on an SDS-PAGE gel and staining with Coomassie blue. Images of the gels were
799 obtained on the BioRad Gel Doc EZ Gel Documentation System with Image Lab™ Software.
800 Representative images are shown. ImageJ was used to quantify the bands, which were plotted in
801 GraphPad Prism.

802 Steady state kinetic analyses were also performed at each pH in 25% PEG 3350. A
803 constant concentration of 2.5 μM TIR was used in these assays. Reaction components were
804 mixed in quadruplicate and incubated at room temperature for 10 min before initiating the reaction
805 with 0-2000 μM of ε-NAD (final concentration). Fluorescence intensity was monitored for 15 min
806 every 15 s. Using the ε-ADPR standard curve, the fluorescence was converted to [ε-ADPR]. The
807 velocity of the reactions was calculated from the slope of the progress curve at each ε-NAD
808 concentration. Kinetic parameters were determined by fitting these velocities to the Michaelis
809 Menten equation (Eq. 1) at each pH. The log of K_m, k_{cat}, and k_{cat}/K_m values were determined and
810 plotted in GraphPad Prism.
811
812 **Negative Stain Electron Microscopy.** Negative stain EM on TIR (270 μg/mL) was performed in
813 Assay Buffer (50 mM Tris, pH 8; 150 mM NaCl) with or without 500 mM sodium citrate. Samples
814 were applied to glow-discharged, carbon- and formvar-coated copper grids and allowed to sit for
815 1 min and 30s before blotting excess liquid away. 1% uranyl acetate was used to fix the samples
816 before image. Samples were images on a FEI Tecnai Spirit 12 microscope. The diameter of
817 particles in the samples with citrate were analyzed in ImageJ.
818
819 **TIR domain mutants.** TIR domain mutants were made using PCR based methods. The pET30a+
820 TIR-1 TIR domain construct was used as a template (0.2-2 ng/μL; final concentration). The
821 manufacturer's protocol for iProof™ High-Fidelity DNA Polymerase (Bio-Rad Laboratories, Inc.)
822 was followed using iProof HF buffer supplemented with 3% DMSO. 50-μL reaction volumes were
823 used in the following protocol: initial denaturation for 3 min at 98 °C, denaturation for 45 s at 98
824 °C, annealing for 1:30 min at 45-72 °C, extension for 6 min at 72 °C, final extension for 10 min at
825 72 °C. Denaturation, annealing, and extension steps were repeated 30 times. The following day,
826 *Dpn*I was added to the PCR reactions and incubated at 37 °C for 2 h to digest the template DNA.
827 The digest was transformed into chemically competent *E. coli* XL1-Blue cells. Transformants were

828 grown overnight in LB media with 50 μg/mL kanamycin and mini-prepped (Promega).
829 Mutagenesis was validated by Sanger sequencing (Genewiz). The mutants were expressed and
830 purified as described for WT TIR.

831 Steady state kinetic analyses of the mutants were carried out in Assay Buffer with 25%
832 PEG 3350 or 500 mM sodium citrate with 2.5 μM of the mutants (final concentrations). Reaction
833 components were mixed in triplicate and incubated at room temperature for 10 min before
834 initiating the reaction with 0-2000 μM of ε-NAD for PEG 3350 or 0-4000 μM for citrate.
835 Fluorescence intensity was monitored for 17.5 min every 15 s. Using the ε-ADPR standard curve,
836 the fluorescence was converted to [ε-ADPR]. The velocity of the reactions was calculated from
837 the slope of the progress curve at each ε-NAD concentration and plotted in GraphPad Prism.
838 Kinetic parameters were determined by fitting these velocities to the Michaelis Menten equation
839 (Eq. 1) for each mutant.

840 To evaluate the precipitation capacity of TIR mutants, 10 μM (WT, G747P, E788Q, and
841 H833A) or 3 μM (WT, E788A) of the enzyme was mixed with Assay Buffer (50 mM Tris, pH 8.0;
842 150 NaCl) with and without 25% PEG 3350 or 500 mM sodium citrate (final concentrations).
843 Precipitation of the TIR^{E788A} mutant was evaluated at 3 μM due to low yields of the protein; WT
844 TIR at 3 μM was included as the proper control. The samples were incubated for 15 min at ambient
845 temperature, at which point the samples were centrifuged at 21,000 *x g* for 10 min at 4 °C. The
846 supernatant was removed, and the pellet was resuspended buffer with the respective additive
847 (final concentration). Samples were diluted 1:1 with water before running on an SDS-PAGE gel.
848 Stain free images of the gels were obtained on the BioRad Gel Doc EZ Gel Documentation
849 System with Image Lab™ Software. Representative images are shown. ImageJ was used to
850 quantify the bands, which were plotted in GraphPad Prism.

851

852 **Statistical Analyses.** Differences in survival of *C. elegans* in the *P. aeruginosa* pathogenesis
853 assays were determined with the log-rank test after survival curves were estimated for each group
854 with the Kaplan-Meier method. OASIS 2 was used for these statistical analyses (84). qRT-PCR
855 studies, intestinal CFU quantification, western blot band intensity quantification, TIR NADase
856 activity, and TIR protein precipitation are presented as the mean ± standard error of the mean.
857 Statistical hypothesis testing was performed with Prism 9 (GraphPad Software) using methods
858 indicated in the figure legends. Sample sizes, mean lifespan, and p-values for all trials are shown
859 in Table S2.

860

861 **Data Availability.** The mRNA-seq dataset is available from the NCBI Gene Expression Omnibus
862 using the accession number GSE178572. All other data are available in the manuscript.

863

REFERENCES

1. W. F. Hieb, M. Rothstein, Sterol requirement for reproduction of a free-living nematode. *Science* **160**, 778-780 (1968).

2. D. J. Chitwood, Biochemistry and function of nematode steroids. *Crit Rev Biochem Mol Biol* **34**, 273-284 (1999).

3. Y. H. Shim, J. H. Chun, E. Y. Lee, Y. K. Paik, Role of cholesterol in germ-line development of *Caenorhabditis elegans*. *Mol Reprod Dev* **61**, 358-366 (2002).

4. M. Merris *et al.*, Sterol effects and sites of sterol accumulation in *Caenorhabditis elegans*: developmental requirement for 4alpha-methyl sterols. *J Lipid Res* **44**, 172-181 (2003).

5. J. Yochem, S. Tuck, I. Greenwald, M. Han, A gp330/megalin-related protein is required in the major epidermis of *Caenorhabditis elegans* for completion of molting. *Development* **126**, 597-606 (1999).

6. B. Otarigho, A. Aballay, Cholesterol Regulates Innate Immunity via Nuclear Hormone Receptor NHR-8. *iScience* **23**, 101068 (2020).

7. M. C. Cheong *et al.*, A potential biochemical mechanism underlying the influence of sterol deprivation stress on *Caenorhabditis elegans* longevity. *J Biol Chem* **286**, 7248-7256 (2011).

8. A. M. Burnell, K. Houthoofd, K. O'Hanlon, J. R. Vanfleteren, Alternate metabolism during the dauer stage of the nematode *Caenorhabditis elegans*. *Exp Gerontol* **40**, 850-856 (2005).

9. J. R. Vanfleteren, A. De Vreese, Rate of aerobic metabolism and superoxide production rate potential in the nematode *Caenorhabditis elegans*. *J Exp Zool* **274**, 93-100 (1996).

10. B. Gerisch, C. Weitzel, C. Kober-Eisermann, V. Rottiers, A. Antebi, A hormonal signaling pathway influencing *C. elegans* metabolism, reproductive development, and life span. *Dev Cell* **1**, 841-851 (2001).

11. B. Gerisch, A. Antebi, Hormonal signals produced by DAF-9/cytochrome P450 regulate *C. elegans* dauer diapause in response to environmental cues. *Development* **131**, 1765-1776 (2004).

12. D. L. Motola *et al.*, Identification of ligands for DAF-12 that govern dauer formation and reproduction in *C. elegans*. *Cell* **124**, 1209-1223 (2006).

13. D. B. Magner *et al.*, The NHR-8 nuclear receptor regulates cholesterol and bile acid homeostasis in *C. elegans*. *Cell Metab* **18**, 212-224 (2013).

14. D. H. Kim *et al.*, A conserved p38 MAP kinase pathway in *Caenorhabditis elegans* innate immunity. *Science* **297**, 623-626 (2002).

899 15. N. T. Liberati *et al.*, Requirement for a conserved Toll/interleukin-1 resistance domain
900 protein in the *Caenorhabditis elegans* immune response. *Proc Natl Acad Sci USA* **101**,
901 6593-6598 (2004).

902 16. C. Couillault *et al.*, TLR-independent control of innate immunity in *Caenorhabditis*
903 *elegans* by the TIR domain adaptor protein TIR-1, an ortholog of human SARM. *Nat.*
904 *Immunol.* **5**, 488-494 (2004).

905 17. E. R. Troemel *et al.*, p38 MAPK regulates expression of immune response genes and
906 contributes to longevity in *C. elegans*. *PLoS Genet* **2**, e183 (2006).

907 18. N. D. Peterson, R. Pukkila-Worley, *Caenorhabditis elegans* in high-throughput screens
908 for anti-infective compounds. *Curr Opin Immunol* **54**, 59-65 (2018).

909 19. R. Pukkila-Worley, F. M. Ausubel, Immune defense mechanisms in the *Caenorhabditis*
910 *elegans* intestinal epithelium. *Curr Opin Immunol* **24**, 3-9 (2012).

911 20. M. Du, Z. J. Chen, DNA-induced liquid phase condensation of cGAS activates innate
912 immune signaling. *Science* **361**, 704-709 (2018).

913 21. D. Chen *et al.*, Inositol Polyphosphate Multikinase Inhibits Liquid-Liquid Phase
914 Separation of TFEB to Negatively Regulate Autophagy Activity. *Dev Cell* **55**, 588-602
915 e587 (2020).

916 22. S. Alberti, A. Gladfelter, T. Mittag, Considerations and Challenges in Studying Liquid-
917 Liquid Phase Separation and Biomolecular Condensates. *Cell* **176**, 419-434 (2019).

918 23. S. Boeynaems *et al.*, Protein Phase Separation: A New Phase in Cell Biology. *Trends*
919 *Cell Biol* **28**, 420-435 (2018).

920 24. S. Alberti, D. Dormann, Liquid-Liquid Phase Separation in Disease. *Annu Rev Genet* **53**,
921 171-194 (2019).

922 25. A. Patel *et al.*, A Liquid-to-Solid Phase Transition of the ALS Protein FUS Accelerated by
923 Disease Mutation. *Cell* **162**, 1066-1077 (2015).

924 26. V. Verdile, E. De Paola, M. P. Paronetto, Aberrant Phase Transitions: Side Effects and
925 Novel Therapeutic Strategies in Human Disease. *Front Genet* **10**, 173 (2019).

926 27. S. Kroschwald *et al.*, Promiscuous interactions and protein disaggregases determine the
927 material state of stress-inducible RNP granules. *Elife* **4**, e06807 (2015).

928 28. S. Brenner, The genetics of *Caenorhabditis elegans*. *Genetics* **77**, 71-94 (1974).

929 29. R. P. Shivers, T. Kooistra, S. W. Chu, D. J. Pagano, D. H. Kim, Tissue-specific activities
930 of an immune signaling module regulate physiological responses to pathogenic and
931 nutritional bacteria in *C. elegans*. *Cell Host Microbe* **6**, 321-330 (2009).

932 30. D. D. Bolz, J. L. Tenor, A. Aballay, A conserved PMK-1/p38 MAPK is required in
933 caenorhabditis elegans tissue-specific immune response to *Yersinia pestis* infection. *J*
934 *Biol Chem* **285**, 10832-10840 (2010).

935 31. T. H. Lindblom, G. J. Pierce, A. E. Sluder, A *C. elegans* orphan nuclear receptor
936 contributes to xenobiotic resistance. *Curr Biol* **11**, 864-868 (2001).

937 32. N. D. Peterson *et al.*, The nuclear hormone receptor NHR-86 controls anti-pathogen
938 responses in *C. elegans*. *PLoS Genet* **15**, e1007935 (2019).

939 33. R. P. Shivers *et al.*, Phosphorylation of the conserved transcription factor ATF-7 by
940 PMK-1 p38 MAPK regulates innate immunity in *Caenorhabditis elegans*. *PLoS Genet* **6**,
941 e1000892 (2010).

942 34. H. Inoue *et al.*, The *C. elegans* p38 MAPK pathway regulates nuclear localization of the
943 transcription factor SKN-1 in oxidative stress response. *Genes Dev* **19**, 2278-2283
944 (2005).

945 35. D. H. Kim *et al.*, Integration of *Caenorhabditis elegans* MAPK pathways mediating
946 immunity and stress resistance by MEK-1 MAPK kinase and VHP-1 MAPK phosphatase.
947 *Proc Natl Acad Sci USA* **101**, 10990-10994 (2004).

948 36. J. R. Powell, D. H. Kim, F. M. Ausubel, The G protein-coupled receptor FSHR-1 is
949 required for the *Caenorhabditis elegans* innate immune response. *Proc Natl Acad Sci U*
950 *S A* **106**, 2782-2787 (2009).

951 37. D. A. Garsin *et al.*, Long-lived *C. elegans daf-2* mutants are resistant to bacterial
952 pathogens. *Science* **300**, 1921 (2003).

953 38. C. F. Chuang, C. I. Bargmann, A Toll-interleukin 1 repeat protein at the synapse
954 specifies asymmetric odorant receptor expression via ASK1 MAPKKK signaling. *Genes*
955 *Dev* **19**, 270-281 (2005).

956 39. S. Horsefield *et al.*, NAD(+) cleavage activity by animal and plant TIR domains in cell
957 death pathways. *Science* **365**, 793-799 (2019).

958 40. L. Wan *et al.*, TIR domains of plant immune receptors are NAD(+)-cleaving enzymes that
959 promote cell death. *Science* **365**, 799-803 (2019).

960 41. D. W. Summers, D. A. Gibson, A. DiAntonio, J. Milbrandt, SARM1-specific motifs in the
961 TIR domain enable NAD+ loss and regulate injury-induced SARM1 activation. *Proc Natl*
962 *Acad Sci U S A* **113**, E6271-e6280 (2016).

963 42. K. Essuman *et al.*, The SARM1 Toll/Interleukin-1 Receptor Domain Possesses Intrinsic
964 NAD(+) Cleavage Activity that Promotes Pathological Axonal Degeneration. *Neuron* **93**,
965 1334-1343.e1335 (2017).

966 43. G. Gadda, P. Sobrado, Kinetic Solvent Viscosity Effects as Probes for Studying the
967 Mechanisms of Enzyme Action. *Biochemistry* **57**, 3445-3453 (2018).

968 44. S. C. Blacklow, R. T. Raines, W. A. Lim, P. D. Zamore, J. R. Knowles, Triosephosphate
969 isomerase catalysis is diffusion controlled. Appendix: Analysis of triose phosphate
970 equilibria in aqueous solution by 31P NMR. *Biochemistry* **27**, 1158-1167 (1988).

971 45. H. S. Loring, V. L. Czech, J. D. Icso, L. O'Connor, S. Parelkar, A. B. Byrne, and P. R.
972 Thompson, A Phase Transition Enhances the Catalytic Activity of SARM1, an NAD+
973 glycohydrolase involved in neurodegeneration. *eLife* **in press** (2021).

974 46. G. Rivas, A. P. Minton, Macromolecular Crowding In Vitro, In Vivo, and In Between.
975 *Trends Biochem Sci* **41**, 970-981 (2016).

976 47. T. R. Peskett *et al.*, A Liquid to Solid Phase Transition Underlying Pathological
977 Huntingtin Exon1 Aggregation. *Mol Cell* **70**, 588-601 e586 (2018).

978 48. N. Pujol *et al.*, Distinct innate immune responses to infection and wounding in the *C.*
979 *elegans* epidermis. *Curr Biol* **18**, 481-489 (2008).

980 49. E. Tecle *et al.*, The purine nucleoside phosphorylase *pnp-1* regulates epithelial cell
981 resistance to infection in *C. elegans*. *PLoS Pathog* **17**, e1009350 (2021).

982 50. K. J. Foster *et al.*, Innate Immunity in the *C. elegans* Intestine Is Programmed by a
983 Neuronal Regulator of AWC Olfactory Neuron Development. *Cell Rep* **31**, 107478
984 (2020).

985 51. Z. Wu *et al.*, Dietary Restriction Extends Lifespan through Metabolic Regulation of Innate
986 Immunity. *Cell Metab* **29**, 1192-1205 e1198 (2019).

987 52. S. M. Anderson, R. Pukkila-Worley, Immunometabolism in *Caenorhabditis elegans*.
988 *PLoS Pathog* **16**, e1008897 (2020).

989 53. A. E. Sluder, S. W. Mathews, D. Hough, V. P. Yin, C. V. Maina, The nuclear receptor
990 superfamily has undergone extensive proliferation and diversification in nematodes.
991 *Genome Res* **9**, 103-120 (1999).

992 54. A. E. Sluder, C. V. Maina, Nuclear receptors in nematodes: themes and variations.
993 *Trends Genet* **17**, 206-213 (2001).

994 55. H. S. Loring, J. D. Icso, V. V. Nemmara, P. R. Thompson, Initial Kinetic Characterization
995 of Sterile Alpha and Toll/Interleukin Receptor Motif-Containing Protein 1. *Biochemistry*
996 **59**, 933-942 (2020).

997 56. J. Gerdts, D. W. Summers, Y. Sasaki, A. DiAntonio, J. Milbrandt, Sarm1-mediated axon
998 degeneration requires both SAM and TIR interactions. *J Neurosci* **33**, 13569-13580
999 (2013).

1000 57. J. Gerdts, D. W. Summers, J. Milbrandt, A. DiAntonio, Axon Self-Destruction: New Links
1001 among SARM1, MAPKs, and NAD+ Metabolism. *Neuron* **89**, 449-460 (2016).

1002 58. J. Gerdts, E. J. Brace, Y. Sasaki, A. DiAntonio, J. Milbrandt, SARM1 activation triggers
1003 axon degeneration locally via NAD(+) destruction. *Science* **348**, 453-457 (2015).

1004 59. M. Carty *et al.*, Cell Survival and Cytokine Release after Inflammasome Activation Is
1005 Regulated by the Toll-IL-1R Protein SARM. *Immunity* **50**, 1412-1424.e1416 (2019).

1006 60. T. Mizuno *et al.*, The *Caenorhabditis elegans* MAPK phosphatase VHP-1 mediates a
1007 novel JNK-like signaling pathway in stress response. *EMBO J* **23**, 2226-2234 (2004).

1008 61. R. Pukkila-Worley, R. L. Feinbaum, D. L. McEwan, A. L. Conery, F. M. Ausubel, The
1009 evolutionarily conserved mediator subunit MDT-15/MED15 links protective innate
1010 immune responses and xenobiotic detoxification. *PLoS Pathog* **10**, e1004143 (2014).

1011 62. L. G. Rahme *et al.*, Common virulence factors for bacterial pathogenicity in plants and
1012 animals. *Science* **268**, 1899-1902 (1995).

1013 63. S. M. Anderson *et al.*, The fatty acid oleate is required for innate immune activation and
1014 pathogen defense in *Caenorhabditis elegans*. *PLoS Pathog* **15**, e1007893 (2019).

1015 64. M. Nandakumar, M. W. Tan, Gamma-Linolenic and Stearidonic Acids Are Required for
1016 Basal Immunity in *Caenorhabditis elegans* through Their Effects on p38 MAP Kinase
1017 Activity. *PLoS Genet* **4**, e1000273 (2008).

1018 65. G. A. Dokshin, K. S. Ghanta, K. M. Piscopo, C. C. Mello, Robust Genome Editing with
1019 Short Single-Stranded and Long, Partially Single-Stranded DNA Donors in
1020 *Caenorhabditis elegans*. *Genetics* **210**, 781-787 (2018).

1021 66. K. S. Ghanta, C. C. Mello, Melting dsDNA Donor Molecules Greatly Improves Precision
1022 Genome Editing in *Caenorhabditis elegans*. *Genetics* **216**, 643-650 (2020).

1023 67. K. Labun *et al.*, CHOPCHOP v3: expanding the CRISPR web toolbox beyond genome
1024 editing. *Nucleic Acids Res* **47**, W171-W174 (2019).

1025 68. A. Fire *et al.*, Potent and specific genetic interference by double-stranded RNA in
1026 *Caenorhabditis elegans*. *Nature* **391**, 806-811 (1998).

1027 69. L. Timmons, D. L. Court, A. Fire, Ingestion of bacterially expressed dsRNAs can produce
1028 specific and potent genetic interference in *Caenorhabditis elegans*. *Gene* **263**, 103-112
1029 (2001).

1030 70. D. Conte, Jr., L. T. MacNeil, A. J. M. Walhout, C. C. Mello, RNA Interference in
1031 *Caenorhabditis elegans*. *Curr Protoc Mol Biol* **109**, 26 23 21-26 23 30 (2015).

1032 71. M. W. Tan, S. Mahajan-Miklos, F. M. Ausubel, Killing of *Caenorhabditis elegans* by
1033 *Pseudomonas aeruginosa* used to model mammalian bacterial pathogenesis. *Proc Natl*
1034 *Acad Sci USA* **96**, 715-720 (1999).

1035 72. K. J. Foster, D. L. McEwan, R. Pukkila-Worley, Measurements of Innate Immune
1036 Function in *C. elegans*. *Methods Mol Biol* **2144**, 145-160 (2020).

1037 73. K. J. Foster, D. L. McEwan, R. Pukkila-Worley, "Measurements of Innate Immune
1038 Function in *C. elegans*" in Methods in Molecular Biology (Aging), S. P. Curran, Ed.
1039 (Springer Nature, New York, NY, 2020), vol. 2144, pp. in press.

1040 74. J. Singh, A. Aballay, Microbial Colonization Activates an Immune Fight-and-Flight
1041 Response via Neuroendocrine Signaling. *Dev Cell* **49**, 89-99 e84 (2019).

1042 75. N. L. Bray, H. Pimentel, P. Melsted, L. Pachter, Near-optimal probabilistic RNA-seq
1043 quantification. *Nat Biotechnol* **34**, 525-527 (2016).

1044 76. H. Pimentel, N. L. Bray, S. Puente, P. Melsted, L. Pachter, Differential analysis of RNA-
1045 seq incorporating quantification uncertainty. *Nat Methods* **14**, 687-690 (2017).

1046 77. A. Subramanian *et al.*, Gene set enrichment analysis: a knowledge-based approach for
1047 interpreting genome-wide expression profiles. *Proc Natl Acad Sci U S A* **102**, 15545-
1048 15550 (2005).

1049 78. M. Fletcher, E. J. Tillman, V. L. Butty, S. S. Levine, D. H. Kim, Global transcriptional
1050 regulation of innate immunity by ATF-7 in *C. elegans*. *PLoS Genet* **15**, e1007830 (2019).

1051 79. S. Taubert, M. Hansen, M. R. Van Gilst, S. B. Cooper, K. R. Yamamoto, The Mediator
1052 subunit MDT-15 confers metabolic adaptation to ingested material. *PLoS Genet* **4**,
1053 e1000021 (2008).

1054 80. C. E. Richardson, T. Kooistra, D. H. Kim, An essential role for XBP-1 in host protection
1055 against immune activation in *C. elegans*. *Nature* **463**, 1092-1095 (2010).

1056 81. K. A. Estes, T. L. Dunbar, J. R. Powell, F. M. Ausubel, E. R. Troemel, bZIP transcription
1057 factor zip-2 mediates an early response to *Pseudomonas aeruginosa* infection in
1058 *Caenorhabditis elegans*. *Proc Natl Acad Sci U S A* **107**, 2153-2158 (2010).

1059 82. M. W. Pfaffl, A new mathematical model for relative quantification in real-time RT-PCR.
1060 *Nucleic Acids Res* **29**, e45 (2001).

1061 83. H. K. Cheesman *et al.*, Aberrant Activation of p38 MAP Kinase-Dependent Innate
1062 Immune Responses Is Toxic to *Caenorhabditis elegans*. *G3 (Bethesda)* **6**, 541-549
1063 (2016).

1064 84. S. K. Han *et al.*, OASIS 2: online application for survival analysis 2 with features for the
1065 analysis of maximal lifespan and healthspan in aging research. *Oncotarget* **7**, 56147-
1066 56152 (2016).
1067

1068 **Figure 1. Cholesterol scarcity activates intestinal innate immune defenses.** Images of
1069 T24B8.5*p::gfp* **(A)** and *irg-5*p*::GFP* **(B)** transcriptional immune reporters in wild-type animals
1070 growing on standard nematode growth media (+5 µg/mL cholesterol) and in the absence of
1071 supplemented cholesterol (+0 µg/mL cholesterol). **(C)** qRT-PCR data of the indicated innate
1072 immune effector genes in wild-type *C. elegans* growing in the presence (+5 µg/mL) and absence
1073 (+0 µg/mL) of supplemented cholesterol. * equals $p<0.05$ (unpaired t-test). **(D)** Data from an
1074 mRNA-seq experiment comparing genes differentially regulated in uninfected *nhr-8(hd117)*
1075 mutants versus wild-type animals (y-axis) are compared with genes differentially expressed in
1076 wild-type animals during *P. aeruginosa* infection (x-axis). All genes are shown in gray. Genes that
1077 are differentially expressed in both datasets are shown in black (Fold change > 2, $q<0.01$). Genes
1078 that are annotated as innate immune genes are shown in red. The location of the representative
1079 genes T24B8.5, *irg*-5, irg-*4*, and K08D8.4, whose expression is examined throughout this
1080 manuscript are shown. See also Table S1. **(E, F, G)** Images of T24B8.5*p::gfp* animals of the
1081 indicted genotypes, grown under the indicated conditions are shown. In Fig. 1*G*, *C. elegans* were
1082 grown on media solidified with agarose, rather than agar. **(H, I, J, K)** qRT-PCR data of the
1083 indicated genes in wild-type and *nhr-8(hd117)* mutant animals grown on standard nematode
1084 growth media (+5 µg/mL cholesterol) in the presence or absence of 0.1% Tergitol, as indicated.
1085 For the qRT-PCR studies in Fig. 1*C, 1H, 1I, 1J, and 1K***,** data are the average of three independent
1086 biological replicates, each normalized to a control gene with error bars representing SEM, and
1087 are presented as the value relative to the average expression from all replicates of the indicated
1088 gene in wild-type animals on standard nematode growth media (+5 µg/mL cholesterol). * equals
1089 $p<0.05$ (two-way ANOVA with Tukey multiple comparison testing). **(L, M)** *C. elegans*
1090 pathogenesis assay with *P. aeruginosa* and *C. elegans* of indicated genotypes at the L4 larval
1091 stage is shown and exposed to the indicated conditions. Data are representative of three trials.
1092 The Kaplan-Meier method was used to estimate the survival curves for each group, and the log
1093 rank test was used for all statistical comparisons. Sample sizes, mean lifespan and p-values for

1094 all trials are shown in Table S2. **(N)** *P. aeruginosa,* isolated from the intestines of animals with the
1095 indicated genotypes, were quantified after 24 hours of bacterial infection. Data are colony forming
1096 units (CFU) of *P. aeruginosa* and are presented as the average of 10 separate biological
1097 replicates with each replicate containing 10-11 animals. * equals $p<0.05$ (unpaired t-test). Scale
1098 bars in all images equals 200 μm. See also Fig. S1.

1099 **Figure 2. Cholesterol scarcity activates the p38 PMK-1 innate immune pathway. (A)** An
1100 immunoblot analysis of lysates from wild-type *C. elegans* grown on standard nematode growth
1101 media in the presence (+5 μg/mL cholesterol) and in the absence (+0 μg/mL cholesterol) of
1102 supplemented cholesterol using antibodies that recognize the doubly phosphorylated TGY motif
1103 of PMK-1 (phospho-PMK-1), total PMK-1 protein (total PMK-1) and tubulin (α-tubulin) is shown.
1104 PMK-1 is a 43.9 kDa protein and tubulin is a 50 kDa protein. **(B)** The band intensities of four
1105 biological replicates of the Western blot shown in Fig. 2*A* were quantified. * equals $p<0.05$
1106 (unpaired t-test) **(C)** Gene set enrichment analysis (GSEA) of p38 PMK-1 targets in the mRNA-
1107 seq experiment. Fold change in expression of significantly differentially expressed genes (fold-
1108 change > 2 and $q<0.01$) in *nhr-8(hd117)* mutants vs. wild-type (in the absence of pathogen
1109 infection) are ranked from higher expression (red) to lower expression (blue) in the *nhr-8(hd117)*
1110 mutant. Normalized enrichment score (NES) and q-value are indicated. p38 PMK-1 targets found
1111 in the transcriptional profile are indicated by hit number (112) in the left margin and black lines.
1112 **(D**, **E)** Western blot experiment and quantification of four biological replicate experiments as
1113 described in Fig. 2*A*. and Fig. 2*B* with the strains of the indicated genotypes. In Fig. 2*A*. and Fig.
1114 2*D***,** *pmk-1(km25)* and *nsy-1(ag3)* and loss-of-function mutants are the controls, which confirm
1115 specificity of phospho-PMK-1 and total PMK-1 probing. * equals $p<0.05$ (one-way ANOVA with
1116 Dunnett multiple comparison testing). **(F)** Images of T24B8.5*p::gfp* transcriptional immune
1117 reporter animals in wild-type animals and *nhr-8(hd117)* mutants growing on control RNAi, *tir-*
1118 *1(RNAi)* or *atf-7(RNAi)* bacteria, as indicated. **(G, H, I, J)** qRT-PCR data of the indicated genes in
1119 the indicated mutant animals grown on standard nematode growth media (+5 μg/mL cholesterol).
1120 Data are the average of three to seven independent replicates, each normalized to a control gene
1121 with error bars representing SEM and are presented as the value relative to the average
1122 expression from all replicates of the indicated gene in wild-type animals. * equals $p<0.05$ (one-
1123 way ANOVA with Dunnett multiple comparison testing) **(K)** Images of T24B8.5*p::gfp*

1124 transcriptional immune reporter animals of the indicated genotypes growing in the presence or

1125 absence of 0.1% Tergitol. Scale bars in all images equals 200 μm. See also Fig. S2.

1126 **Figure 3. Activation of the p38 PMK-1 pathway by cholesterol deprivation requires TIR-1**
1127 **oligomerization and NADase activity. (A)** Model of *tir-1* showing the domains and the mutations
1128 that were introduced using CRISPR-Cas9. **(B, C)** Expression of the innate immune effector
1129 T24B8.5p::*gfp* in *tir-1* mutants with predicted defects in oligomerization (*tir-1*$^{\Delta SAM}$, *tir-1*^{G747P} and *tir-*
1130 *1*^{H833A}) and NADase catalytic activity (*tir-1*^{E788A}) in the indicated genetic backgrounds and
1131 conditions. Scale bars in all images equals 200 μm. **(D)** Immunoblot analysis of lysates from the
1132 indicated genotypes probed with antibodies targeting the doubly phosphorylated TGY epitope in
1133 phosphorylated PMK-1 (phos-PMK-1), total PMK-1, and tubulin. *nsy-1(ag3)* and *pmk-1(km25)*
1134 loss-of-function mutants are the controls, which confirm the specificity of the phospho-PMK-1
1135 probing. **(E)** The band intensities of three biological replicates of the Western blot shown in **(D)**
1136 were quantified. * equals $p<0.05$ (one-way ANOVA with Dunnett multiple comparison testing). **(F)**
1137 qRT-PCR data of T24B8.5 in wild-type and mutant animals of the indicated genotypes grown on
1138 standard nematode growth media (+5 μg/mL cholesterol). Data are the average of three
1139 independent replicates, each normalized to a control gene with error bars representing SEM and
1140 are presented as the value relative to the average expression from all replicates in wild-type
1141 animals. * equals $p<0.05$ (two-way ANOVA with Tukey multiple comparison testing). **(G)** *C.*
1142 *elegans* pathogenesis assay with *P. aeruginosa* and *C. elegans* of indicated genotypes at the L4
1143 larval stage are shown. Data are representative of three trials. The Kaplan-Meier method was
1144 used to estimate the survival curves for each group, and the log rank test was used for all
1145 statistical comparisons. Sample sizes, mean lifespan and p-values for all trials are shown in Table
1146 S2. See also Fig. S3.

1147 **Figure 4. The NAD^+ glycohydrolase activity of TIR-1/SARM1 is activated by a phase**
1148 **transition that requires TIR oligomerization. (A)** NADase activity of purified TIR at increasing
1149 TIR protein concentrations is shown. Activity was assessed by incubating TIR protein with 1 mM
1150 ε-NAD and monitoring the rate at which the fluorescent product ε-ADPR was produced. Curve
1151 represents a nonlinear regression fit of the NADase activity data points (n=2). **(B)** NADase activity
1152 of 2.5 μM TIR incubated in the presence of 25% (w/v) of macro- (PEG 8000, PEG 3350 and
1153 dextran) and micro- (sucrose and glycerol) viscogens was assessed as described in Fig. 4*A* (n=2).
1154 **(C)** Dose dependency of macroviscogens on the NADase activity of TIR is shown. 2.5 μM TIR
1155 protein was incubated with the indicated PEG compound at concentrations from 0-30% (w/v).
1156 NADase activity was assessed as described in Fig. 4*A* (n=2). **(D)** Steady-state kinetic analysis of
1157 2.5 μM TIR incubated in 0-30% (w/v) of PEG 3350 with the ε-NAD substrate provided at
1158 concentrations from 0-4000 μM was assessed as described in Fig. 4*A*. (n=2). From the steady-
1159 state kinetic analysis performed in Fig. 4*D*, K_m **(E)**, k_{cat} **(F)**, and k_{cat}/K_m **(G)** were determined at
1160 each PEG 3350 concentration. **(H)** SDS-PAGE analysis of TIR protein fractions incubated with
1161 increasing concentrations of PEG 3350 before [precentrifugation (C)] and after centrifugation, the
1162 soluble (S) and pellet (P) protein fractions. NADase activity of TIR protein in each fraction and at
1163 each concentration of PEG 3350 was assessed, as described in Fig. 4*A* and is represented below
1164 the gel image (n=2, representative image shown). **(I)** Steady-state kinetic analysis of TIR wild-
1165 type, oligomerization mutant (TIR^{G747P}), and catalytic mutants (TIR^{E788Q} and TIR^{E788A}) in 25% PEG
1166 3350 assessed with 0-2000 μM ε-NAD was assessed as described in Fig. 4*D*. Kinetic parameters
1167 (K_m, k_{cat} and k_{cat}/K_m) are shown in the table below the graph (n=3). **(J, K)** SDS-PAGE analysis of
1168 TIR: wild-type, oligomerization mutant (TIR^{G747P}) and catalytic mutants (TIR^{E788Q} and TIR^{E788A}),
1169 precipitation in the presence of 25% PEG 3350. Gel represents the soluble (S) and pellet (P)
1170 protein fractions of wild-type and mutant TIR following incubation with PEG 3350 and
1171 centrifugation. TIR^{G747P} and TIR^{E788Q} were assessed with 10 μM protein in Fig. 4*J* and TIR^{E788A}
1172 was assessed with 3 μM protein in Fig. 4*K*. Quantification of replicates represented below gel

1173 images (n=4, representative images shown). * equals $p<0.05$ by one-way ANOVA in Fig. 4*J* and

1174 unpaired t-test in Fig. 4*K*. See also Fig. S4.

1175 **Figure 5. A phase transition superactivates the intrinsic NAD+ glycohydrolase of TIR. (A)**
1176 Effect of 1,6-hexanediol on TIR NADase activity is shown. TIR protein was incubated in the
1177 presence or absence of either 25% PEG 3350 or 500 mM citrate, and treated with either 0 or 2%
1178 1,6-hexanediol. The NADase activity of TIR for each condition was assessed using the ε-NAD
1179 substrate assay (n=3). * equals $p<0.05$ (unpaired t-test). **(B)** The NADase activity of TIR protein
1180 incubated with either 25% PEG 3350 or 500 mM citrate before (precentrifugation, n=2) and after
1181 centrifugation, the supernatant (n=4) and precipitant (n=2) fractions. Precipitation fractions were
1182 resuspended in buffer alone or buffer containing 25% PEG 3350 or 500 mM citrate and NADase
1183 activity assessed. **(C)** SDS-PAGE analysis of TIR protein in the soluble (S) and pellet (P) fractions
1184 following incubation with either PEG 3350 or citrate and centrifugation (1 spin). Pellet fractions
1185 were subsequently resuspended in only buffer or buffer containing 25% PEG 3350 or 500 mM
1186 citrate and centrifuged a second time to isolate the soluble (S) and pellet (P) fractions (n=2,
1187 representative image shown). **(D)** SDS-PAGE analysis of TIR in the soluble (S) and pellet (P)
1188 fractions incubated with or without 25% PEG 3350 at the indicated pH (n=2, representative image
1189 shown). TIR steady state kinetic parameters [K_m **(E)**, k_{cat} **(F)**, k_{cat}/K_m **(G)**] is shown at the indicated
1190 pH (n=2). **(H)** Negative stain electron microscopy in either the absence or presence of 500 mM
1191 citrate (diameter of particles = 8.9 nm ± 1.2, n = 65). See also Fig. S5.

1192 **Figure 6. Sterol scarcity primes p38 PMK-1 immune defenses. (A ,B, C, D, E)** Images of the
1193 indicated transcriptional immune reporters under the indicated conditions. Scale bars in all images
1194 equals 200 μm. **(F)** A heat map compares the expression levels of the 184 genes that were both
1195 induced in wild-type animals during *P. aeruginosa* infection and differentially expressed (either
1196 induced or repressed) in *nhr-8(hd117)* mutants at baseline (each greater than 2-fold, q<0.05). To
1197 compare expression of these genes in wild-type and *nhr-8(hd117)* mutants, we scaled the
1198 expression level in each condition by calculating a z-score for each row and performed
1199 hierarchical clustering, which identified two main clusters (Cluster I has 139 genes and Cluster II
1200 contains 45 genes). See also Table S3. **(G)** Enrichment of p38 PMK-1-dependent genes in Cluster
1201 I and II genes is shown. **(H, I, J, K)** mRNA-seq data for the indicated genes from the experiment
1202 described in 6*F* showing scaled reads per base from three biological replicates. * equals q<0.05
1203 from RNA-seq analysis. **(L)** Model of p38 PMK-1 pathway activation during sterol scarcity.

1204 **Supplementary Figure 1. Cholesterol scarcity activates intestinal innate immune defenses.**
1205 **(A)** An mRNA-seq experiment as described in Fig. 1*D*, except using a different *nhr-8* mutant allele:
1206 *nhr-8(ok186)*. **(B)** Images of T24B8.5p::*gfp* animals as described in Fig. 1*F*. **(C)** Images of
1207 T24B8.5p::*gfp* on agarose media with 0.1% Tergitol in the presence of supplemented fatty acids,
1208 as indicated. **(D, E, F, G)** Pathogenesis assay with *P. aeruginosa* and *C. elegans* of indicated
1209 genotypes at the L4 larval stage is shown. Data are representative of three trials. The Kaplan-
1210 Meier method was used to estimate the survival curves for each group, and the log rank test was
1211 used for all statistical comparisons. Sample sizes, mean lifespan and p-values for all trials are
1212 shown in Table S2. Scale bars in all images equals 200 μm. See also Fig. 1.

1213 **Supplementary Figure 2. Cholesterol scarcity activates the p38 PMK-1 innate immune**
1214 **pathway. (A)** Gene set enrichment analysis (GSEA) of p38 PMK-1 targets in the mRNA-seq
1215 experiment as described in Fig 2*C*, except using a different *nhr-8* mutant allele: *nhr-8(ok186)*. **(B)**
1216 Images of T24B8.5p::*gfp* animals, as described in Fig. 2*F*. **(C)** Images of the transgenic *C.*
1217 *elegans*, in which *gfp* has been fused to the DAF-16 protein under the indicated conditions. Scale
1218 bars in all images equals 200 μm. See also Fig. 2.

1219 **Supplementary Figure 3. Activation of the p38 PMK-1 pathway by cholesterol deprivation**
1220 **requires TIR-1 oligomerization and NADase activity. (A)** qRT-PCR data of *irg-4* in wild-type
1221 and mutant animals as described in Fig. 3C. **(B)** Immunoblot analysis of lysates from the indicated
1222 genotypes probed with an antibody that recognizes the FLAG epitope. **(C)** Images of
1223 T24B8.5p::*gfp* immune reporter containing the indicated genotypes. Scale bars in all images
1224 equals 200 μm. See also Fig. 3.

1225 **Supplementary Figure 4. (A)** Enzyme concentration dependence in presence and absence of
1226 either 25% PEG 3350 or 500 mM sodium citrate (n=2). **(B)** Dose dependence of TIR NADase
1227 activity on citrate concentration as described in Fig. 4*C*, except using citrate (n=2). **(C)** Steady-
1228 state kinetic analysis of TIR as described in Fig. 4*D*, except in the presence of citrate (n=2). **(D-**
1229 **F)** From the steady-state kinetic analysis performed in **(C)**, K_m **(D)**, k_{cat} **(E)**, and k_{cat}/K_m **(F)** were
1230 determined at each citrate concentration. **(G)** Effect of citrate on TIR aggregation and associated
1231 activity as described in Fig. 4*H* (n=2, representative images shown). **(H)** Steady state kinetic
1232 analysis of TIR mutants as described in Fig. 4*I*, except in the presence of citrate (n=3). **(I, J)**
1233 Precipitation of TIR mutants as described in Fig. 4*J* and 4*K*, except in the presence of citrate (n=4,
1234 representative images shown). See also Fig. 4.

1235 **Supplementary Figure 5. (A)** SDS-PAGE analysis of TIR protein soluble (S) and pellet (P)
1236 fractions following TIR incubation first with 25% PEG 3350 or 500 mM citrate and subsequently
1237 addition of 2% 1,6-hexanediol (n=2, representative image shown). **(B)** SDS-PAGE analysis of TIR
1238 protein soluble (S) and pellet (P) fractions following TIR incubation first with 0 or 2% 1,6-
1239 hexanediol and subsequently addition of 25% PEG 3350 or 500 mM citrate (n=2, representative
1240 image shown). See also Fig. 5.

1241 **Supplementary Table S1. Genes differentially expressed in *nhr-8(hd117)* and *nhr-8(ok186)***
1242 **mutants compared to wild-type in the RNA-seq experiment presented in Fig. 1*D* and S1*A*.**
1243
1244 **Supplementary Table S2. Sample sizes, mean lifespan, and p values for the *C. elegans***
1245 **pathogenesis assays.**
1246
1247 **Supplementary Table S3. Genes in Cluster 1 and Cluster 2 of the heat map shown in Fig.**
1248 **6*F*.**
1249
1250 **Supplementary Table S4. Primer, crRNA guide and ssODN sequences designed for this**
1251 **study.**
1252

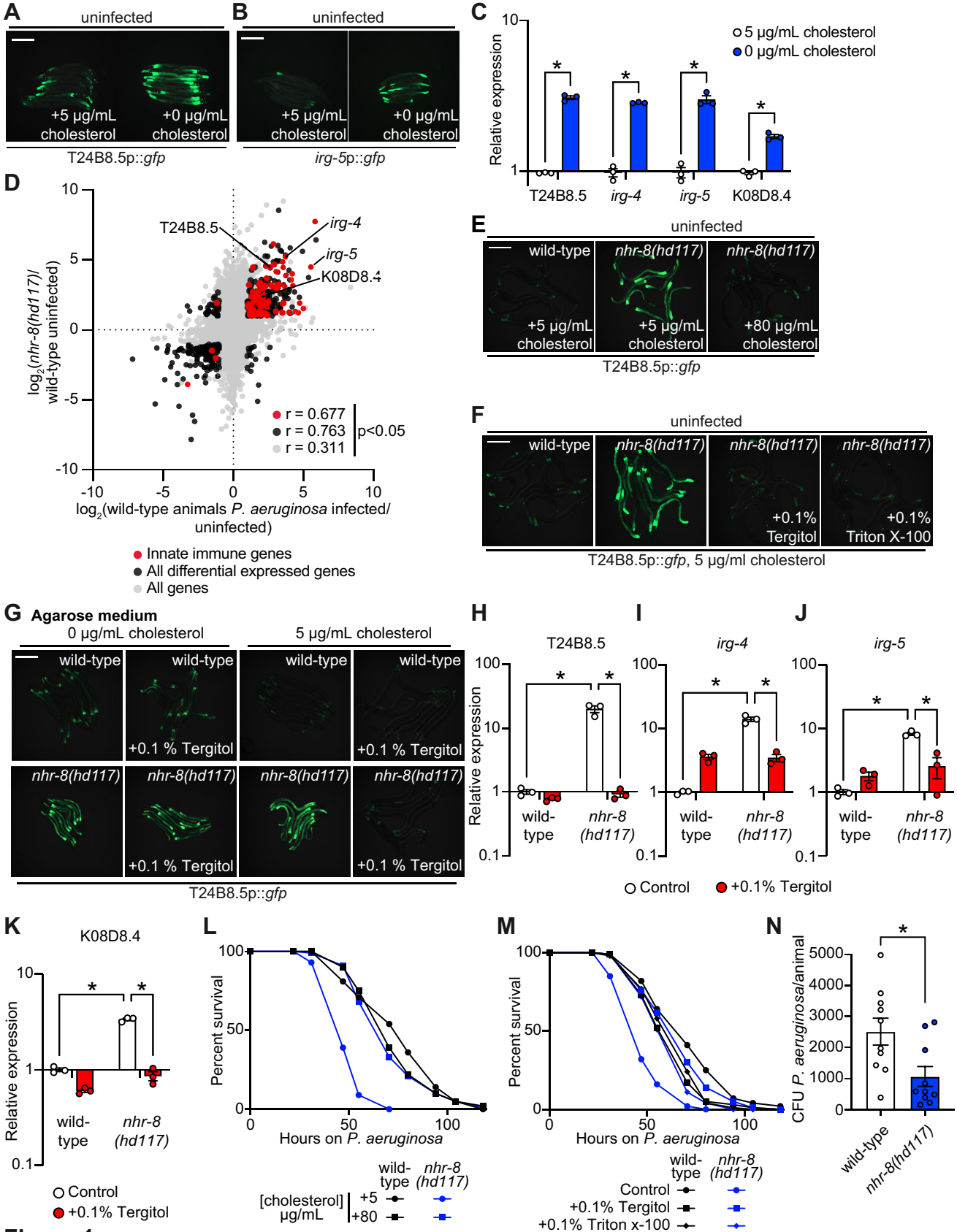
A
uninfected
+5 µg/mL cholesterol
+0 µg/mL cholesterol
T24B8.5p::gfp
B
uninfected
+5 µg/mL cholesterol
+0 µg/mL cholesterol
irg-5p::gfp
C
5 µg/mL cholesterol
0 µg/mL cholesterol
Relative expression
T24B8.5
irg-4
irg-5
K08D8.4
D
T24B8.5
irg-4
irg-5
K08D8.4
log2(nhr-8(hd117)/ wild-type uninfected)
log2(wild-type animals P. aeruginosa infected/ uninfected)
r = 0.677
r = 0.763
r = 0.311
p<0.05
Innate immune genes
All differential expressed genes
All genes
E
uninfected
wild-type
nhr-8(hd117)
nhr-8(hd117)
+5 µg/mL cholesterol
+5 µg/mL cholesterol
+80 µg/mL cholesterol
T24B8.5p::gfp
F
uninfected
wild-type
nhr-8(hd117)
nhr-8(hd117)
nhr-8(hd117)
+0.1% Tergitol
+0.1% Triton X-100
T24B8.5p::gfp, 5 µg/ml cholesterol
G
Agarose medium
0 µg/mL cholesterol
5 µg/mL cholesterol
wild-type
+0.1 % Tergitol
nhr-8(hd117)
T24B8.5p::gfp
H
T24B8.5
I
irg-4
J
irg-5
Relative expression
wild-type
nhr-8 (hd117)
Control
+0.1% Tergitol
K
K08D8.4
Relative expression
wild-type
nhr-8 (hd117)
Control
+0.1% Tergitol
L
Percent survival
Hours on P. aeruginosa
wild-type
nhr-8 (hd117)
[cholesterol] µg/mL
+5
+80
M
Percent survival
Hours on P. aeruginosa
wild-type
nhr-8 (hd117)
Control
+0.1% Tergitol
+0.1% Triton x-100
N
CFU P. aeruginosa/animal
wild-type
nhr-8(hd117)

Figure 1

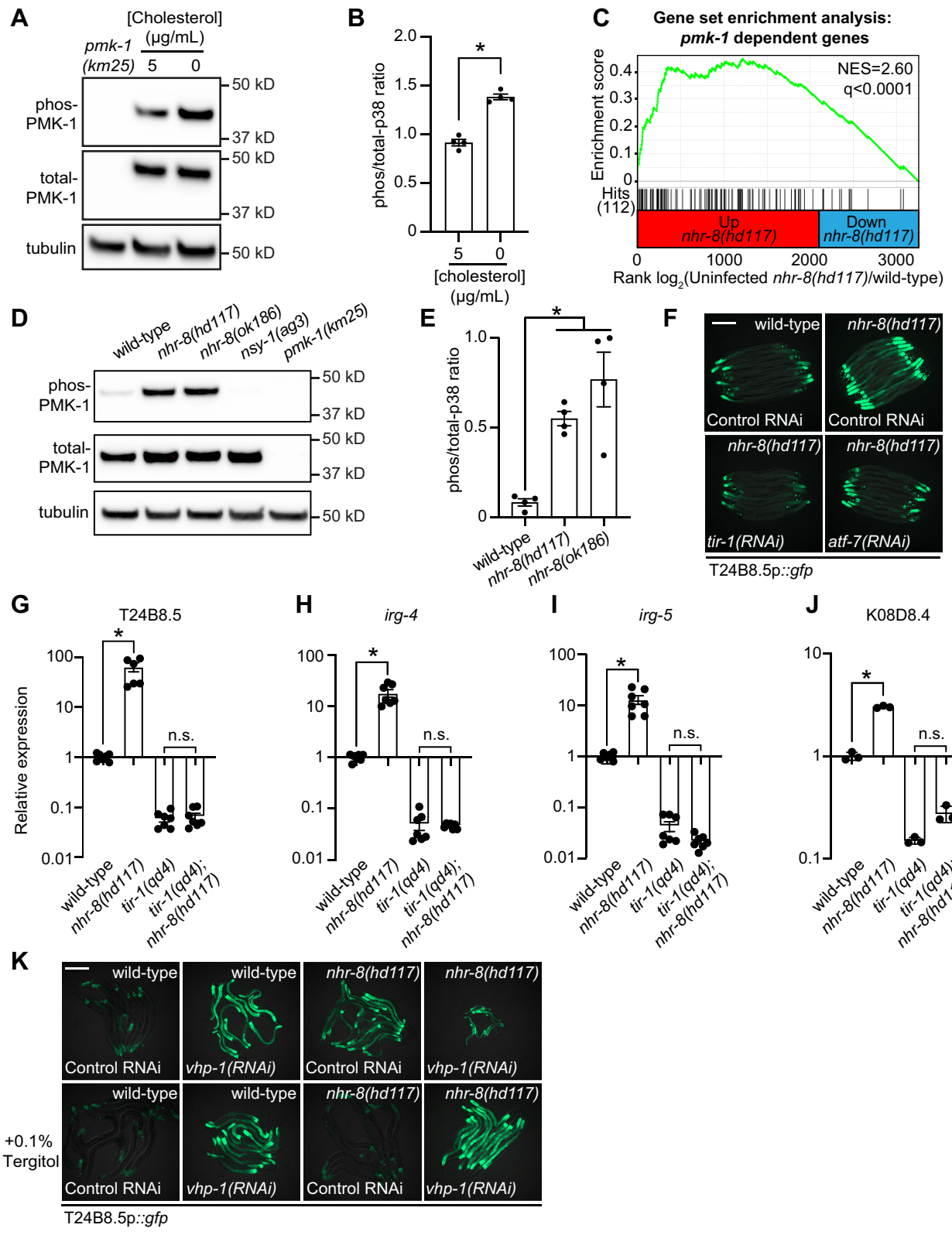
A
[Cholesterol] (µg/mL)
pmk-1 (km25)
5
0
phos-PMK-1
total-PMK-1
tubulin
50 kD
37 kD
B
phos/total-p38 ratio
[cholesterol] (µg/mL)
C
Gene set enrichment analysis: pmk-1 dependent genes
Enrichment score
NES=2.60
q<0.0001
Hits (112)
Up nhr-8(hd117)
Down nhr-8(hd117)
Rank log2(Uninfected nhr-8(hd117)/wild-type)
D
wild-type
nhr-8(hd117)
nhr-8(ok186)
nsy-1(ag3)
pmk-1(km25)
E
F
Control RNAi
tir-1(RNAi)
atf-7(RNAi)
T24B8.5p::gfp
G
T24B8.5
Relative expression
n.s.
H
irg-4
I
irg-5
J
K08D8.4
tir-1(qd4)
tir-1(qd4); nhr-8(hd117)
K
vhp-1(RNAi)
+0.1% Tergitol

Figure 2

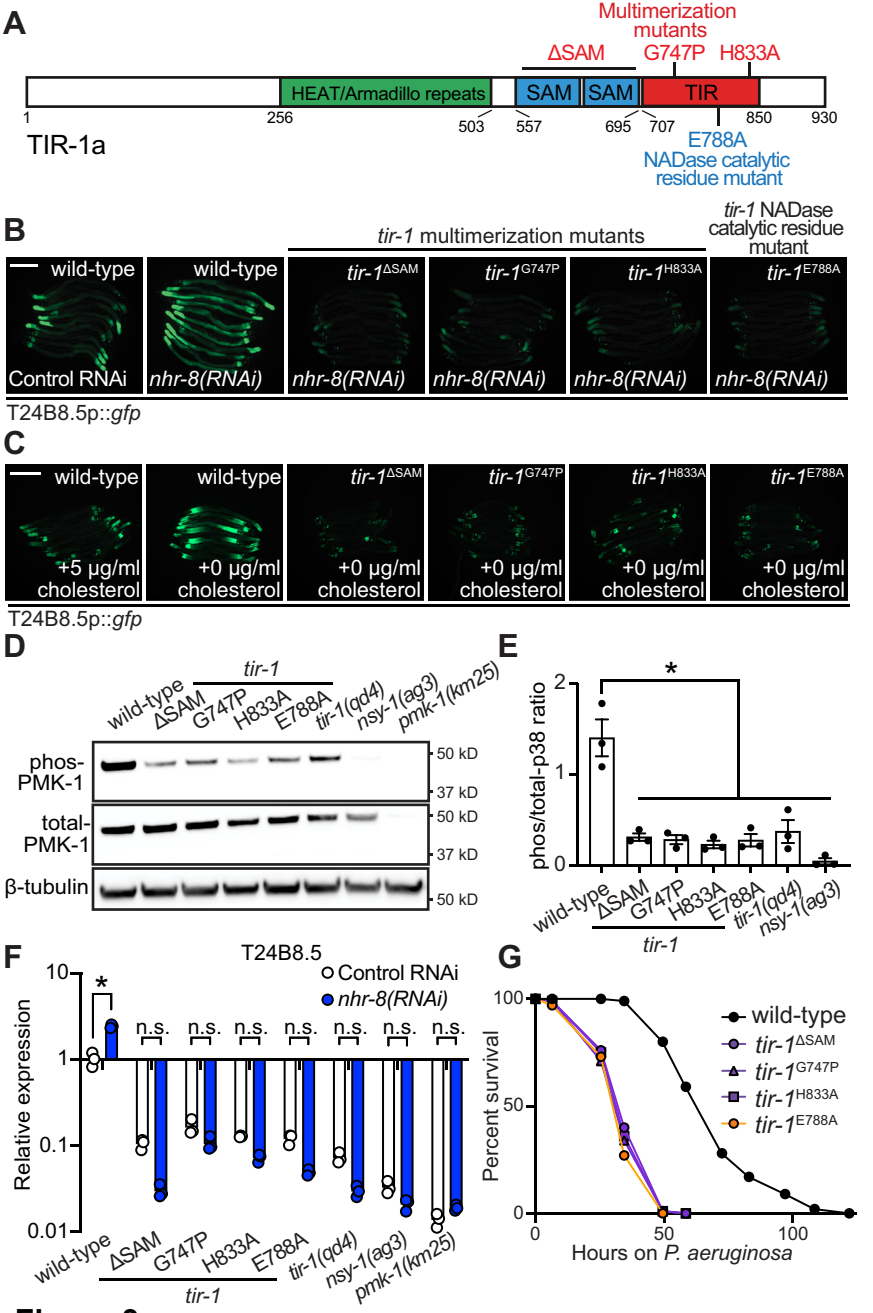
A
Multimerization mutants
ΔSAM
G747P
H833A
HEAT/Armadillo repeats
SAM
SAM
TIR
1
256
503
557
695
707
850
930
TIR-1a
E788A
NADase catalytic residue mutant
B
tir-1 multimerization mutants
tir-1 NADase catalytic residue mutant
wild-type
wild-type
tir-1ΔSAM
tir-1G747P
tir-1H833A
tir-1E788A
Control RNAi
nhr-8(RNAi)
nhr-8(RNAi)
nhr-8(RNAi)
nhr-8(RNAi)
nhr-8(RNAi)
T24B8.5p::gfp
C
wild-type
wild-type
tir-1ΔSAM
tir-1G747P
tir-1H833A
tir-1E788A
+5 µg/ml cholesterol
+0 µg/ml cholesterol
+0 µg/ml cholesterol
+0 µg/ml cholesterol
+0 µg/ml cholesterol
+0 µg/ml cholesterol
T24B8.5p::gfp
D
tir-1
wild-type
ΔSAM
G747P
H833A
E788A
tir-1(qd4)
nsy-1(ag3)
pmk-1(km25)
phos-PMK-1
total-PMK-1
β-tubulin
50 kD
37 kD
50 kD
37 kD
50 kD
E
phos/total-p38 ratio
2
1
0
*
wild-type
ΔSAM
G747P
H833A
E788A
tir-1(qd4)
nsy-1(ag3)
tir-1
F
T24B8.5
Control RNAi
nhr-8(RNAi)
Relative expression
10
1
0.1
0.01
*
n.s.
wild-type
ΔSAM
G747P
H833A
E788A
tir-1(qd4)
nsy-1(ag3)
pmk-1(km25)
tir-1
G
Percent survival
100
50
0
0
50
100
Hours on P. aeruginosa
wild-type
tir-1ΔSAM
tir-1G747P
tir-1H833A
tir-1E788A

Figure 3

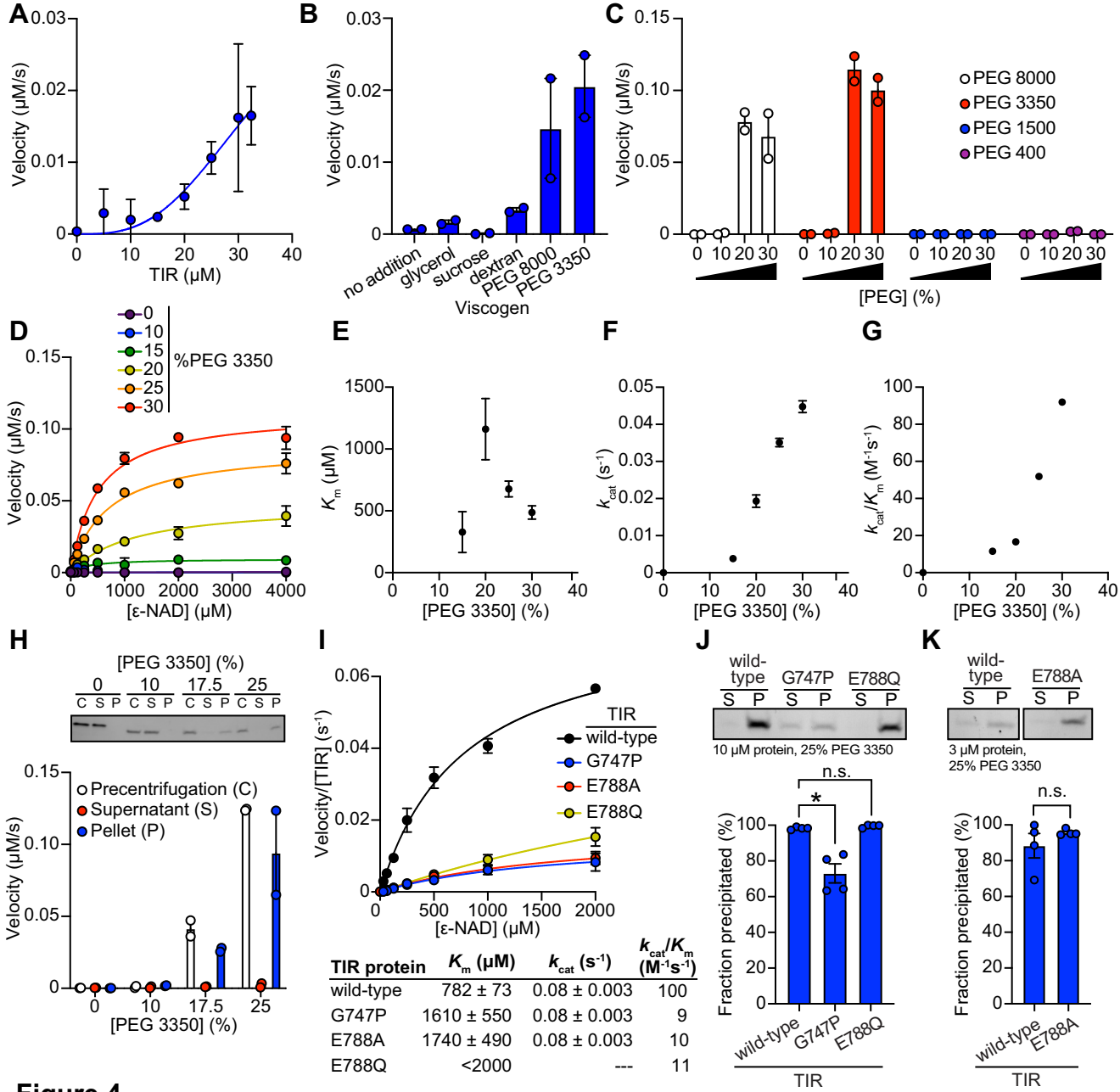

TIR protein	K_m (μM)	k_{cat} (s^{-1})	k_{cat}/K_m (M^{-1}s^{-1})
wild-type	782 ± 73	0.08 ± 0.003	100
G747P	1610 ± 550	0.08 ± 0.003	9
E788A	1740 ± 490	0.08 ± 0.003	10
E788Q	<2000	---	11

Figure 4

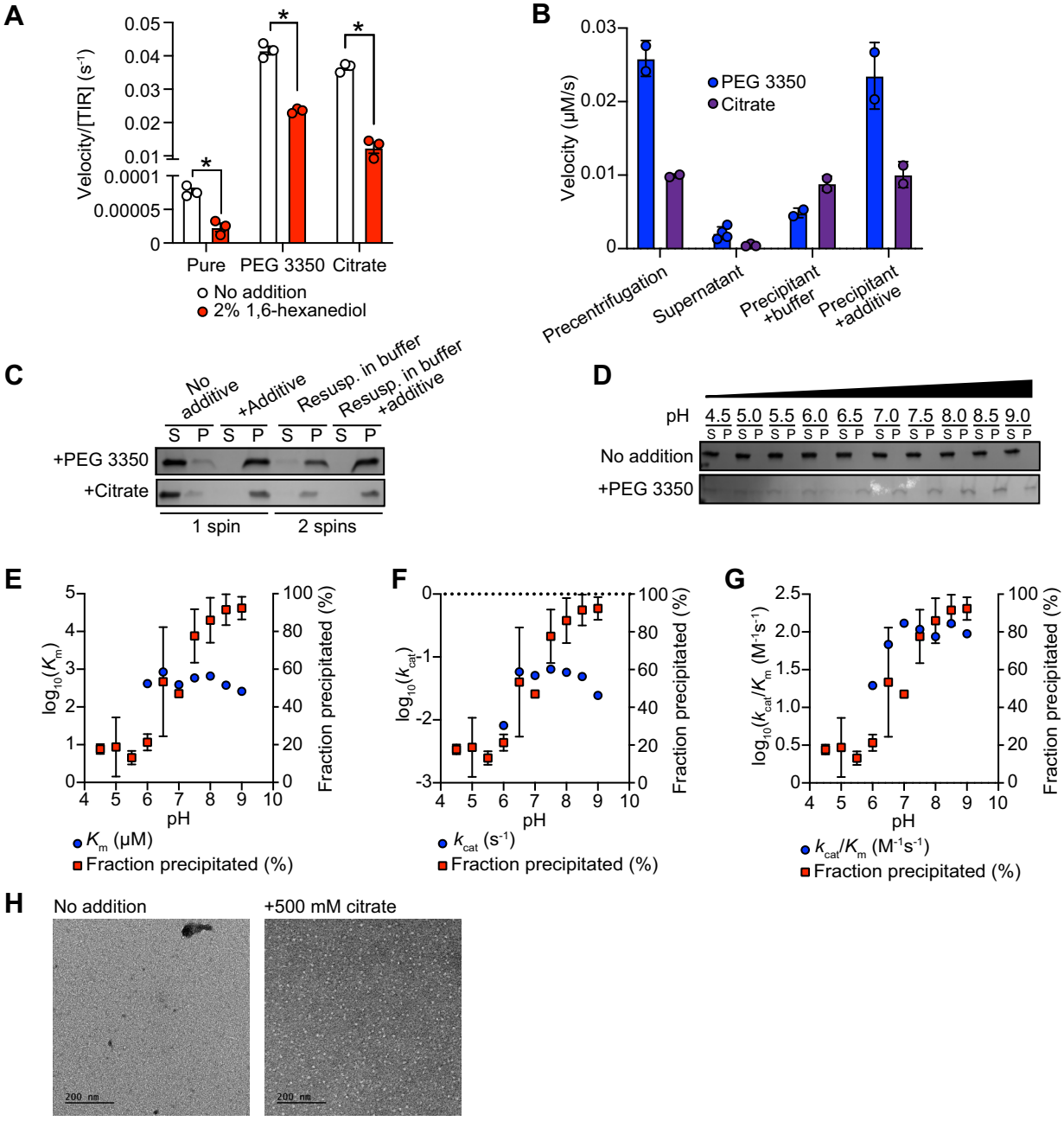
A
Velocity/[TIR] (s-1)
0.05
0.04
0.03
0.02
0.01
0.0001
0.00005
0
*
Pure
PEG 3350
Citrate
No addition
2% 1,6-hexanediol
B
Velocity (μM/s)
0.03
0.02
0.01
0
PEG 3350
Citrate
Precentrifugation
Supernatant
Precipitant +buffer
Precipitant +additive
C
No additive
+Additive
Resusp. in buffer
Resusp. in buffer +additive
S P S P S P S P
+PEG 3350
+Citrate
1 spin
2 spins
D
pH 4.5 5.0 5.5 6.0 6.5 7.0 7.5 8.0 8.5 9.0
No addition
+PEG 3350
E
log10(Km)
Fraction precipitated (%)
pH
Km (μM)
Fraction precipitated (%)
F
log10(kcat)
Fraction precipitated (%)
pH
kcat (s-1)
Fraction precipitated (%)
G
log10(kcat/Km (M-1s-1)
Fraction precipitated (%)
pH
kcat/Km (M-1s-1)
Fraction precipitated (%)
H
No addition
+500 mM citrate
200 nm
200 nm

Figure 5

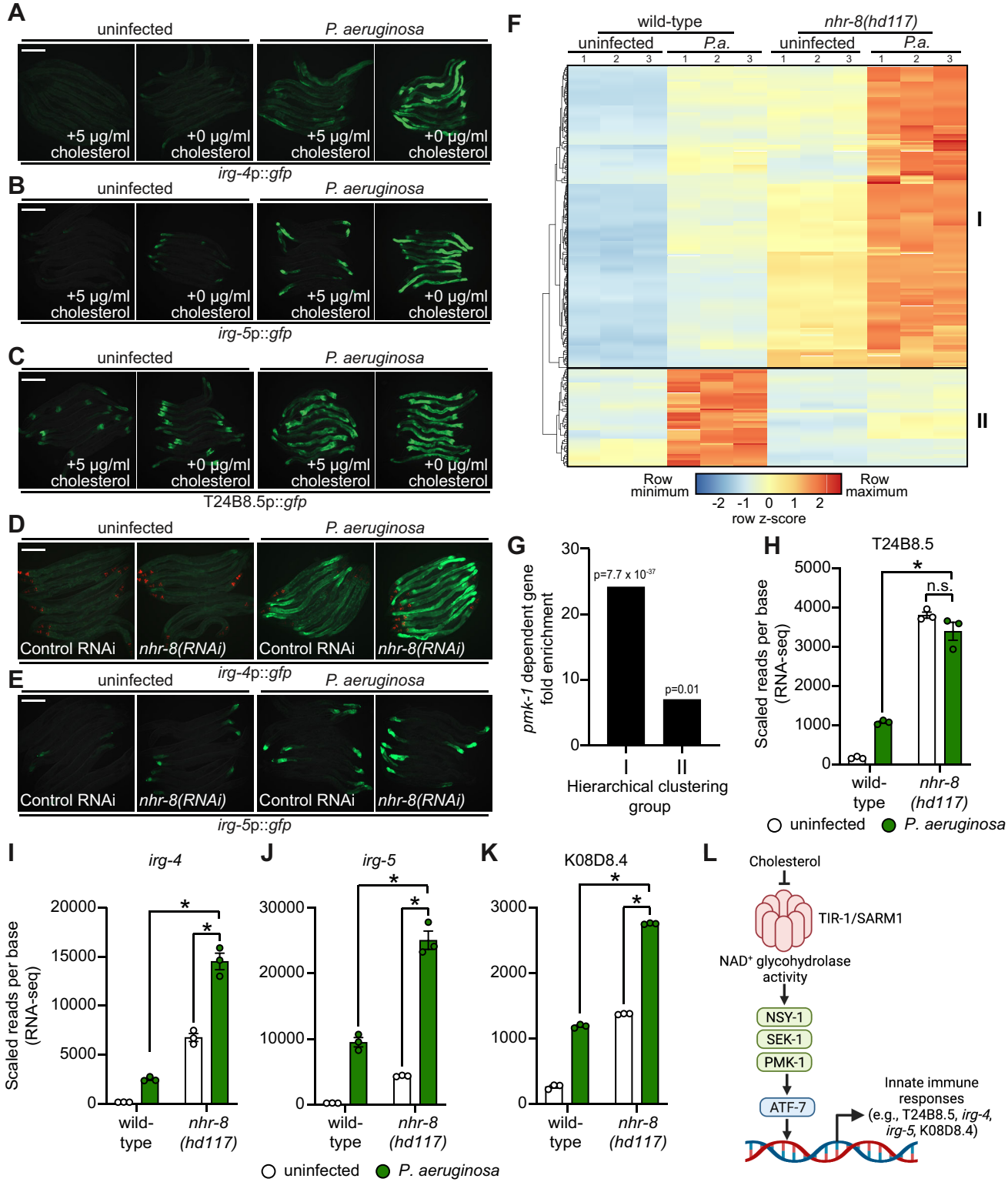
A
uninfected
P. aeruginosa
+5 µg/ml cholesterol
+0 µg/ml cholesterol
irg-4p::gfp
B
irg-5p::gfp
C
T24B8.5p::gfp
D
Control RNAi
nhr-8(RNAi)
E
F
wild-type
nhr-8(hd117)
P.a.
I
II
Row minimum
Row maximum
row z-score
G
pmk-1 dependent gene fold enrichment
p=7.7 x 10-37
p=0.01
Hierarchical clustering group
H
T24B8.5
Scaled reads per base (RNA-seq)
n.s.
wild-type
nhr-8 (hd117)
uninfected
P. aeruginosa
I
irg-4
J
irg-5
K
K08D8.4
L
Cholesterol
TIR-1/SARM1
NAD+ glycohydrolase activity
NSY-1
SEK-1
PMK-1
ATF-7
Innate immune responses (e.g., T24B8.5, irg-4, irg-5, K08D8.4)

Figure 6

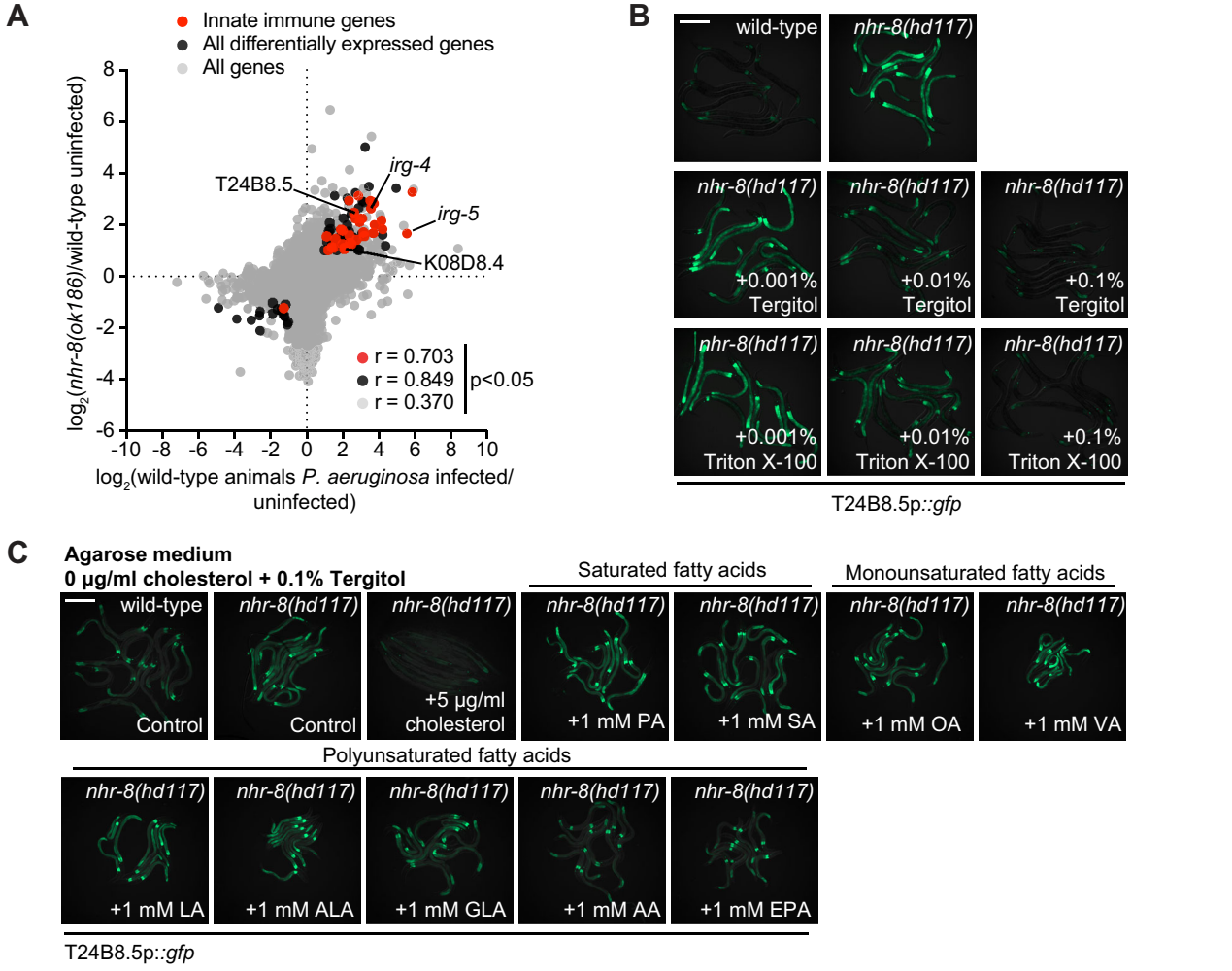

Supplementary Figure 1

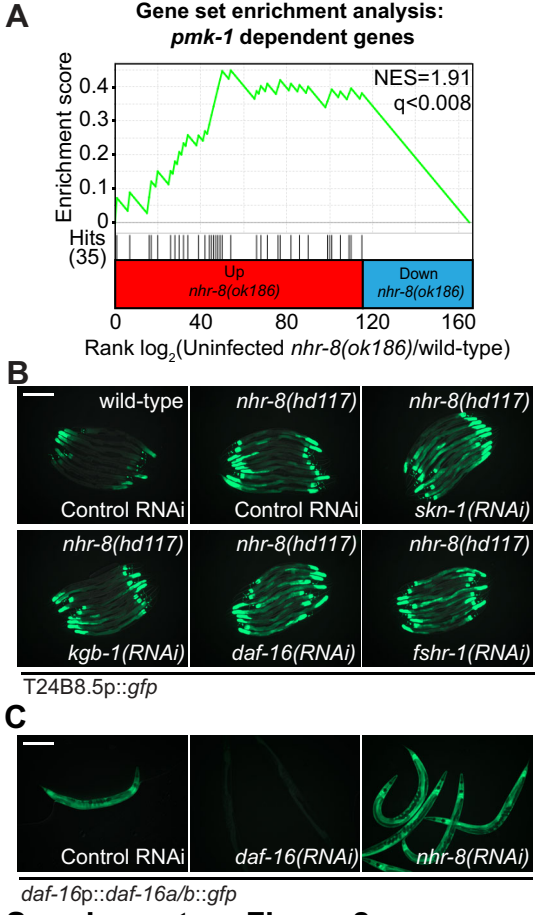

Supplementary Figure 2.

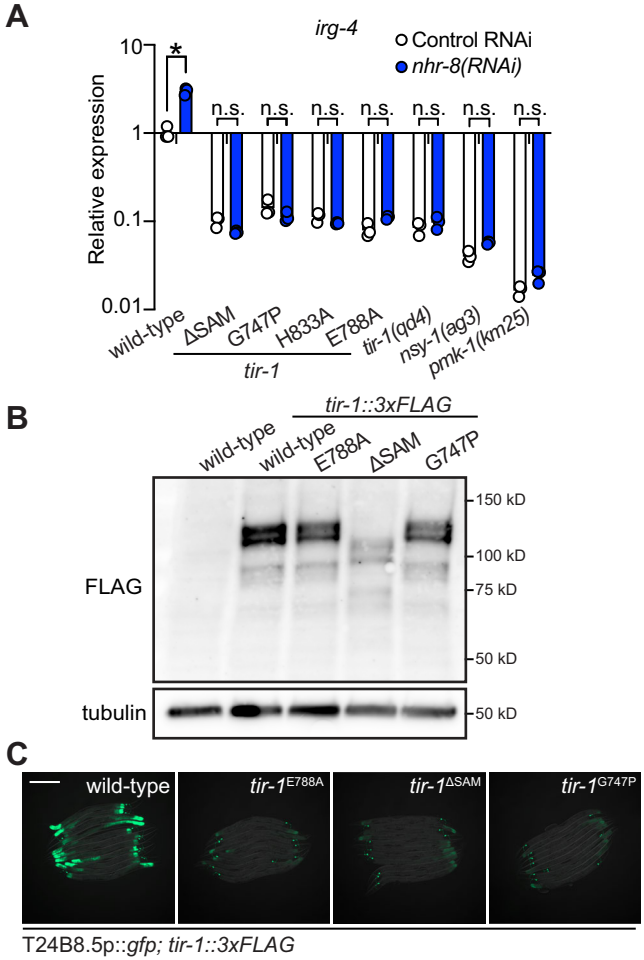

Supplementary Figure 3

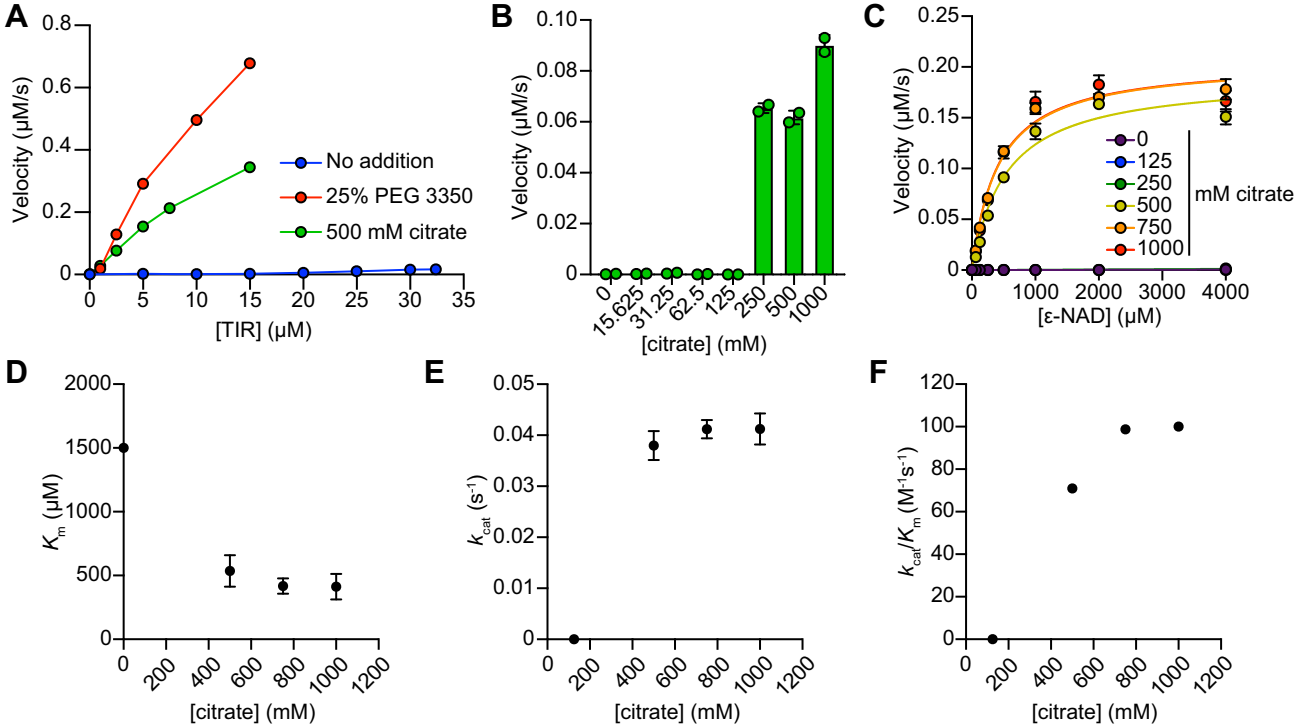

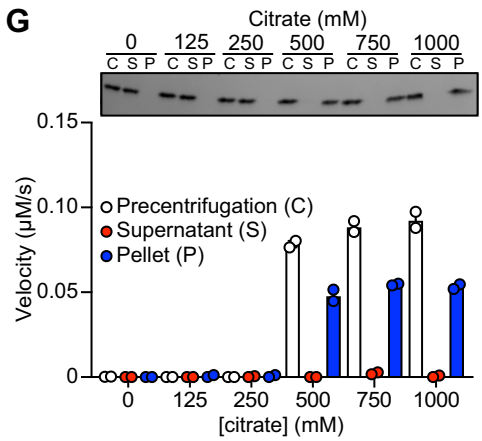

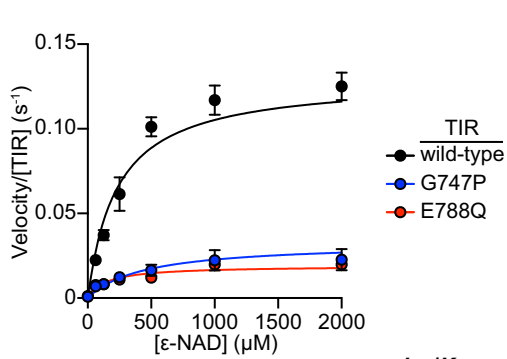

TIR protein	K_m (μM)	k_{cat} (s^{-1})	k_{cat}/K_m ($M^{-1}s^{-1}$)
wild-type	230 ± 73	0.013 ± 0.0006	56
G747P	443 ± 550	0.003 ± 0.0003	7.4
E788A	---	---	---
E788Q*	149 ± 38	0.002 ± 0.0007	13

*No apparent activity detected

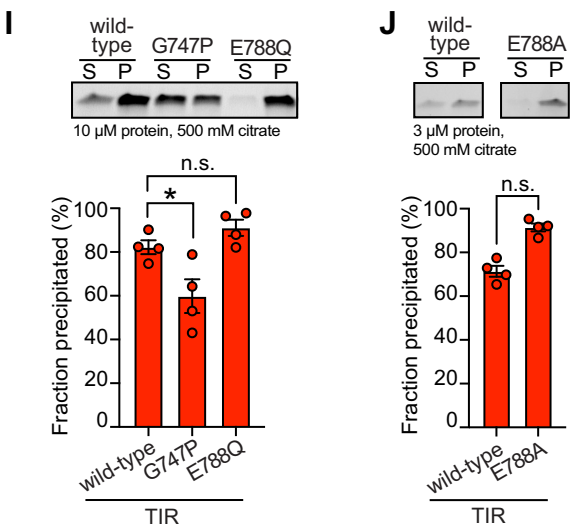

Supplementary Figure 4

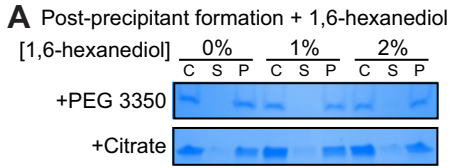

Supplementary Figure 5